Tribological characterization of the additively manufactured 18Ni300 maraging steel

João Miguel Martins Mendes Viseu Coelho

Thesis to obtain the Master of Science Degree in

Mechanical Engineering

Supervisors: Prof. Pedro Alexandre Rodrigues Carvalho Rosa

Prof. Pedro Miguel de Almeida Areias

Examination Committee

Chairperson: Prof. Rui Manuel dos Santos Oliveira Baptista

Supervisor: Prof. Pedro Alexandre Rodrigues Carvalho Rosa

Members of the Committee: Prof. Jorge Manuel da Conceição Rodrigues

Prof. Abílio Manuel Pinho de Jesus

January 2021

“What I love about science is that as you learn, you don’t really get answers. You just get better questions.”

- John Green

Acknowledgements

I want to present the most grateful thanks to the supervisor, Professor Pedro Rosa, and to the co-supervisor, Professor Pedro Areias, for the support, patience, motivation, and for all the knowledge and experience given to me, which will surely be useful in my future personal and professional life.

To all my colleagues and their friendly, but helpful, motivational and professional atmosphere from Laboratory of Machining and Micro Manufacturing (LabM3), specially to Eng.º Pedro Santos.

To our dear colleagues from FEUP, Professor Abilio de Jesus and Tiago Silva, for their immense collaboration.

To Prof. Pedro Mendes, for the thoughtful insights provided.

Throughout the development of this work and the entire degree, to my parents, for the constant interest and motivation, and the most special thanks to Catarina, for the personal support and growth provided, as well as the constant inspiration.

To all my colleagues that crossed my path throughout the degree, which contributed to my personal and professional development.

Institutional Acknowledgments

This work was supported by FCT, through IDMEC, under LAETA, project UIDB/50022/2020.

The project MAMTool entitled “Machinability of Additive Manufactured Parts for Tooling Industry” funded by the Programa Operacional Competitividade e Internacionalização, and Programa Operacional Regional de Lisboa funded by FEDER and National Funds (FCT) is acknowledged (Reference PTDC/EME-EME/31895/2017).

Laboratory of Machining and Micro Manufacturing (LabM3), Instituto Superior Técnico, for proposing the theme of this dissertation and for performing the laboratorial experiments analysed in this work.

Resumo

A crescente necessidade de obter componentes com melhor performance e geometrias mais complexas tem levado ao surgimento de novos materiais de engenharia de alta resistência, como o aço maraging, que pode inclusivamente ser obtido por fabrico aditivo. No entanto, ainda existem poucos estudos sobre a sua caracterização mecânica e principalmente tribológica presentes na literatura.

Assim, esta dissertação apresenta um estudo tribológico acerca do aço maraging 18Ni300 através de duas abordagens distintas: corte ortogonal e ensaios de anel. Ambos os ensaios foram realizados em provetes obtidos por fabrico convencional e aditivo, para comparar o desempenho de ambas as condições metalúrgicas. Os ensaios de anel foram realizados utilizando pratos compressores de baixa rugosidade, para isolar o efeito da adesão no coeficiente de atrito, e em condições de alta temperatura e altas taxas de deformação, para compreender os efeitos de condições operacionais realistas no coeficiente de atrito. Os resultados mostram uma nítida variação do coeficiente de atrito com a temperatura e velocidade (>50%), mas não com o processo de fabrico dos provetes, o que vai de encontro aos resultados obtidos em corte ortogonal. Por outro lado, os ensaios de corte ortogonal mostraram uma variação do coeficiente de atrito com a espessura de corte e com a velocidade de deformação em provetes de maraging obtido por fabrico aditivo.

A presente investigação também introduziu uma abordagem original para a quantificação de atrito a altas temperaturas e velocidades de deformação ao usar uma “Split – Hopkinson Pressure Bar (SHPB)” e pratos de compressão de alta resistência de carboneto de tungsténio, que permitiram efetuar os ensaios com sucesso.

Palavras-Chave: Atrito, Maraging, Fabrico Aditivo, Temperatura, Taxa de Deformação

Abstract

The growing need for better performance and more complex geometries has led to the appearance of new high resistance engineering materials, such as the maraging steel, which can inclusively be additively manufactured. However, few studies about its mechanical and tribological behavior exist in the literature.

This dissertation presents a tribology study on 18Ni300 maraging steel using two different experimental techniques commonly used to assess friction in the manufacturing domain: orthogonal cutting and ring compression tests. Experimental tests were performed on conventional and additively manufactured maraging specimens, to compare the performance of both metallurgical conditions. The ring compression tests were carried out using low roughness compression platens, to isolate the influence of the operative conditions on the friction coefficient, and were performed at different temperatures and strain rates, to better understand the effect of real metal shaping and cutting operations conditions on the friction coefficient. The ring compression tests shown a significant variation of the friction coefficient with temperature and speed (>50%). However, the manufacturing process of the specimens didn't have such a significant influence on the friction coefficient, which is in accordance with the results obtained on the orthogonal cutting tests. On the other hand, the orthogonal cutting tests shown a variation of the friction coefficient with the depth of cut and with strain rate on AM maraging specimens.

The present investigation also introduced an original approach to friction quantification at high temperatures and strain rates by using a Split – Hopkinson Pressure Bar (SHPB) and highly resistant tungsten carbide compression platens, which successfully performed the required high speed and temperature experiments.

Keywords: Friction, Maraging, Additive Manufacturing, Temperature, Strain Rate

Contents

List of tables

List of figures

Abbreviations

AC – *Alternating Current*

AM – *Additive Manufacturing*

CAD – *Computer-Aided Design*

CBN - *Cubic Boron Nitride*

CNC – *Computer Numeric Control*

DAQ – *Data Acquisition*

DC – *Direct Current*

FEM – *Finite Element Method*

FEUP – *Faculdade de Engenharia da Universidade do Porto*

HSS – *High Speed Steel*

IST – *Instituto Superior Técnico*

LPBF – *Laser Powder Bed Fusion*

PCD – *Polycrystalline Diamond*

PMF – *Pure Metal Factor*

QS – *Quasi-static*

SHPB – *Split Hopkinson pressure bar*

SLM – *Selective Laser Melting*

UPS – *Uninterruptible Power Source*

WC – *Tungsten Carbide*

List of symbols

α – Tool rake angle

α_a – Relation between the real and apparent area on the Wanheim-Bay friction model

β – Friction angle

β_a – Percentage of surface contact area between two surfaces

ε – Engineering strain

ε_e – Elastic strain

ϕ – Shear plane angle

μ – Friction coefficient

μ_a – Friction coefficient due to adhesion

μ_f – Friction coefficient due to deformation and/or fracture of surface layers

μ_M – Friction coefficient present on a metal – ceramic interface

$\mu_{máx}$ – Maximum friction coefficient

μ_O – Friction coefficient present on an oxide – ceramic interface

μ_p – Friction coefficient due to plowing

μ_{part} – Friction coefficient due to interference and local deformation induced by third bodies

σ – Normal stress

σ_y – Yield stress

τ – Shear stress

τ_{AB} – Maximum stress on the shear plane

τ_i – Medium stress in the contact surface

$\tau_{máx}$ – Maximum shear stress

b – Specimen's width

e – Depth of cut

e' – Chip thickness

f– Shear stress relative value representation (between 0 to 1)

l_{ct} – Contact length

m – Friction factor

k – Shear stress in the shear plane

p – Pressure normal to the contact surface

A_0 – Cross-sectional area of the undeformed chip

A_f – Area of a ring specimen at the end of a compression test

A_i – Area of a ring specimen before a compression test

E – Elastic Modulus

F_a – Friction force

F_c – Cutting force

F_p – Penetration force

F_N – Force normal to the contact surface

K_s – Specific cutting pressure

P – Percentage of oxide present on the surface of a ring specimen after a compression test

R – Resultant force

R_c – Compression ratio

V_A – Shear plane velocity

V_c – Cutting velocity

V_e – Chip velocity

W – Compressive force applied to a given solid

W' – Normal tensile force required for separation between two solid surfaces

W_c – Cutting power

1. Introduction

In recent years, metal shaping operations and new manufacturing technologies have been developed, as a consequence of the rising needs for better components with higher performance and more complex geometries. Consequently, new high resistance and high-performance engineering materials have been emerging in the last decades, known for their high temperature resistance, high corrosion resistance or high strength to weight ratio. When studying a new material, mechanical resistance, plasticity and microstructural aspects are some of the most analyzed factors. Another important aspect is the quantification of friction, as a performance indicator of mechanical components and determinant factor to reduce energy and wear, despite the lack of studies regarding its analysis present on the literature. This fact, combined to the little knowledge about these new engineering materials, motivates the present study, which focus on the friction coefficient's variation with temperature, speed and metallurgical condition (conventional vs. additively manufactured) on the maraging steel – conventional and additively manufactured.

The maraging steels are known for their superior strength and toughness without losing malleability, due to the precipitation of inter-metallic compounds (Bhukya, *et al.*, 2014). However, this material's characteristics change, with aging. Lohmann *et al.* (2019) found that maraging 300 steel, when aged at 480ºC, 580ºC and 650ºC, produces a rearrangement in the martensite phase, as well as a common occurrence in maraging steels: austenite reversion. The extent of these phenomena depends on the time and temperature of the heat treatment. This steel can also be obtained through SLM (Selective Laser Melting), which gives the additive manufactured (AM) maraging parts high mechanical strength. Some authors studied the effects of ageing on AM maraging steels, which forms strengthening precipitates. Some of these effects include an increase in tensile performances and hardness, but a decrease in toughness (Casati et al., 2016). Other authors (Ansell et al., 2020) also studied the effect of the printing orientation (vertical, 45º and horizontal, relative to the print plate), and found higher ultimate tensile strength in vertical and 45º specimens, but higher tensile properties than conventional maraging steel in all specimens, especially the specimens printed with vertical orientation. The maraging steel is also known to have a bad machinability on the conventional state, but lowers when additively manufactured. Besides this specific material, new engineering material's machinability is generally low, and characterized by extremely high temperatures in the cutting zone, problems in chip formation, bad surface quality generated by the cutting process and deterioration of the subsurface area, which are known factor for excessive wear on cutting tools (Wegener, *et al.*, 2016). Besides the maraging steel, some of the other most known and studied difficult to machine materials include titanium alloys, nickel alloys, cobalt alloys and organic materials, and some common properties they have that contribute to their bad machinability are a low thermal conductivity, high chemical reactivity with tool materials and the formation of built-up edge in the cutting zone.

As mentioned above, there are few studies regarding the tribological characterization of the 18Ni300 steel, both conventional and AM, particularly, when considering high temperature and strain rate conditions. Therefore, the present dissertation intends to evaluate the friction coefficient present on a

maraging steel – tungsten carbide interface at extreme plastic deformation conditions, typical of manufacturing processes, as well as how its value is influenced by significantly different metallurgical conditions (wrought vs additively manufactured material). To provide the pretended tribological characterization and quantification, ring compression tests were performed, and complemented with orthogonal cutting tests on the same material.

Ring compression tests are one of the most widely accepted ways to analyze friction on a given interface, due to its extreme simplicity. For the present work, high speed and temperature conditions were used in order to simulate realistic operating conditions of high strength engineering materials. This test consists of compressing a ring-shaped specimen and measuring its change in height and internal diameter throughout the process, using different tribological conditions (i.e., dry or lubricated). Its simplicity comes from the fact that friction coefficient (μ) can be evaluated only by measuring the changes in the shape of the specimen. The more deformation the material suffers, the higher the friction coefficient (Male, 1965). However, on the present work, the roughness of the compression platens used is very low, promoting the adhesion mechanism. Adhesion is still one of the most complex phenomena to investigators that occur on solid-solid clean interfaces, being mainly activated with lower roughness values. Some suggest that covalent, ionic and metallic bonds are the microscopic causes, being more prevalent than the weaker hydrogen and van der Waals bonds, as stated by Bhushan, 2003. The author still suggests an increase of friction by adhesion with temperature.

Later, some authors started studying the effects of temperature changes in the ring compression test. Shahriari et al. (2011) found an increase on the friction coefficient with temperature (1175ºC ns 1100ºC) when conducting ring compression tests on Nimonic 115 superalloy using different lubricating conditions. The authors still claim that the hot ring compression test (ring compression test performed at high temperatures) is a good way to estimate the flow stress behavior and performance of a lubricant.

Other factor that has driven some attention from investigators is the strain rate effect on the ring compression test. Male (1965) suggests that an increase in the press speed can provide greater lubrication efficiency when using soft or liquid lubricants. Garmong et al. (1977) also states that strain rate sensitive materials are more likely to changes in the friction coefficient when using different test speeds. Other authors (Börder, 2005, Asai, et al., 2017) studied the combined effects of temperature and strain-rate on the friction coefficient. Börder (2005) studied the relative influence of these parameters on the ring compression test using steel specimens and polished compression platens, and concluded that temperature is the most influential factor, followed by the type of tool coating, and finally, speed (strain rate). Asai et al. performed high temperature (1100 ºC) and high speed (50 $mm.s^{-1}$) ring compression tests and reported a slight change in the friction coefficient under those conditions.

Despite the presence of some studies in literature regarding the influence of temperature and strain rate on the friction coefficient, the combined effect of both theses parameters is practically nonexistent. Some authors (Sun, 2020, Opalinski, 2016) used the pin-on-disc test on this material, suggesting that abrasion is the main wear mechanism (Sun, 2020), but very few studies regarding ring compression tests on the maraging steel exist. Consequently, and adding this fact to the relevance of quantifying friction and the

relevance of machinability analysis on new engineering materials, the present work intends to fill these knowledge gaps by tackling the following questions:

- How is the friction coefficient affected by typical temperatures and strain rates of manufacturing processes?
- Out of these parameters, which is the most influential on the friction coefficient?
- Does the additively manufactured steel performance differ from the conventional material?

This thesis is partitioned in six chapters, including the introduction. The second chapter presents the theoretical background relevant to this work, including a tribology physical and theoretical explanation, and the most common ways to evaluate friction: pin-on-disc, ring compression and orthogonal cutting experiments, the last two being the ones used for the present work. Orthogonal cutting tribometers will also be discussed, as one was developed throughout the course of this study. This chapter also contains a section dedicated to the new engineering materials (including the maraging steel). In the third chapter, the experimental methods carried out are presented, including a developed orthogonal cutting tribometer, detailed in all its mechanical and electronic components, as well as the ring compression tests machine and the full plan of experiments. The fourth chapter is dedicated to the FEM simulation models developed, including the compression model (used for strain-stress curves correction), and the ring compression model (used to obtain the calibration curves). The fifth chapter contains the metal cutting tests and the ring compression tests results, as well as their comparison and discussion. Finally, on the sixth and last chapter of this dissertation the conclusions and future works suggested by the author are presented.

2. Theoretical Background

This chapter presents the state of the art and all the fundamental knowledge that supports this research. First, a tribology theoretical and physical explanation will be presented, alongside its most used models. Then, the two chosen ways to assess friction for the present work will be presented in detail: ring compression apparatus and orthogonal cutting tribometers. Finally, in the last section, the additively manufactured metals will be presented, including the maraging steel.

2.1. Tribology

This section presents a theoretical background of tribology. First, the physical aspects of friction will be presented. Then, the most used friction models (Amonton-Coulomb, Prandtl and Wanheim-Bay) will be shown. Finally, the most used methods to quantify the friction coefficient will be presented (namely, the pin-on-disc tests, as the next sections are dedicated to ring compression and orthogonal cutting operations).

2.1.1. Physical Aspects of Friction

Friction is defined as the force that opposes the relative motion between two surfaces in contact. Friction and wear are not basic intrinsic properties of materials, but the feedback of a material pair in a certain environment to imposed forces. The friction force is a dissipative force, and universal agreement about what truly causes friction does not exist, as a number of phenomena and mechanisms are involved, namely fluid mechanics (lubrication), mechanics of deformable solids, material science, surface physics and surface chemistry, thermodynamics, fracture mechanics, etc…

On the other hand, tribology is the science of interacting surfaces in relative motion, and is an interdisciplinary field of study, involving physics, chemistry, metallurgy, elasticity, viscoelasticity, material science, lubrication and heat transfer. Its study has the purpose of reducing wear to conserve energy and increasing productivity and efficiency.

Consequently, frictional interactions occur under a wide variety of contact conditions. This is the reason why selecting test methods of lubricants for frictional behavior should be done carefully.

The basic mechanisms involved in friction are:

1) Plastic deformation and plowing, μ_p: caused by the deformation of one surface by hard asperities existing on the other;
2) Deformation and/or fracture of surface layers (i.e. oxides), μ_f;
3) Interference and local plastic deformation caused by third bodies, μ_{part}, which consist of agglomerations of small wear particles;
4) Adhesion, μ_a, which will be detailed in the upcoming paragraphs, as it is the phenomenon mainly involved on the ring compression experiments performed for the present work.

The total friction coefficient present on a given operation is then given by:

$$\mu = \mu_a + \mu_p + \mu_f + \mu_{part} \quad (1)$$

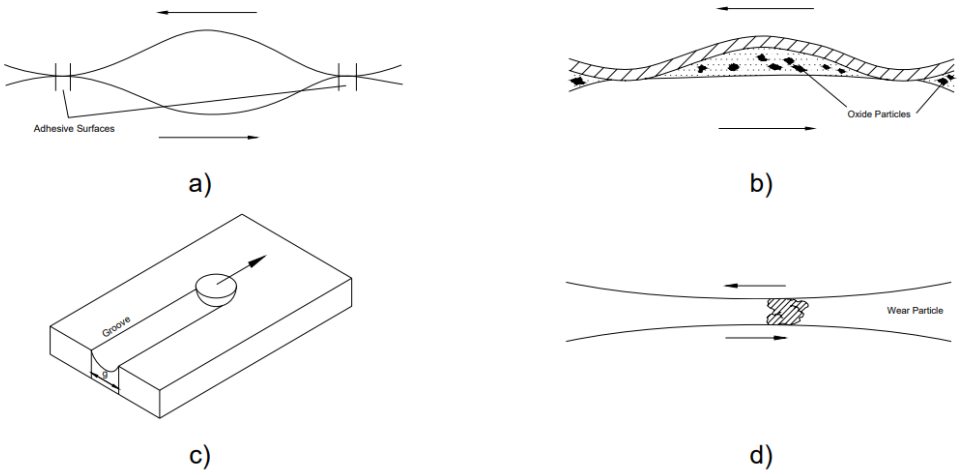

Figure 2-1. Main friction mechanisms, as presented by Cristino (2007): (a) Adhesion; (b) Deformation and fracture of oxides; (c) Plowing; (d) Trapped wear particle

Of all these phenomena presented, adhesion seems to be the most complex among investigators, as it involves a number of physical and chemical phenomena. It occurs when two solid surfaces are brought into contact, and the friction coefficient due to adhesion is given by:

$$\mu_a = \frac{W'}{W} \quad (2)$$

where W' corresponds to the normal tensile force required for separation (also known as adhesive force) and W is the compressive force initially applied. W' typically increases proportionally with an increase of W, and μ_a increases with separation rate and duration of static contact (Bhushan, 2003). Roughness seems to promote a decrease in adhesion, as the real contact area increases. Adhesion can occur in solid-solid interfaces and solid surfaces interspersed with a fluid, but removal of chemical films, adsorbates and other impurities promotes strong adhesion and bonding between two solids.

In terms of the microscopic phenomena that cause adhesion, Bhushan (2003) suggests that covalent, ionic and metallic bonds are the present chemical interactions, and hydrogen and van der Waals bonds are the present physical interactions. However, the last two are not usually the main adhesion mechanisms, as they present a weaker bond than the chemical interactions presented, and strongly depend on interatomic distance. The author still suggests that adhesion increases with temperature, as softening of surfaces results in greater ductility and area of contact, consequently increasing the adhesion friction coefficient. Dubois (2014) also suggests a link between friction and electron transport, while performing pin-on-disc experiments on solid-solid metal interfaces, but claims that many unknowns are present on the adhesion topic, highlighting again the lack of general understanding of the chemical and physical effects on friction.

Other investigators drive their attention to study these phenomena under more extreme conditions. Miyoshi (1995) found a strong adhesive bond on a metal-ceramic interface under high vacuum

experimental conditions, being even a stronger bond than the cohesive bond found in the metal, suggesting the strong contribution that adhesion can have on friction between two surfaces under extreme conditions.

2.1.2. Friction Models

In this subsection, the three most famous theoretical approaches to friction quantification will be presented: the Amonton-Coulomb, Prandtl and Wanhem-Bay models.

The Amonton-Coulomb friction model, also known as the classical friction model, states that the friction coefficient is given by:

$$\mu = \frac{F_a}{F_N} = \frac{\tau_i}{\sigma_N} \tag{3}$$

where μ is the friction coefficient, F_N is the force perpendicular to the contact surface, F_a is the resulting friction force, τ_i the mean shear stress on the contact surface and σ_N the normal contact pressure. In this model, the friction coefficient is independent of the real and apparent contact areas between two surfaces.

This friction model is the one that will be used in the FEA software, to simulate the uniaxial compression and ring compression tests, due to its simplicity and adequacy to the problem being studied.

Another relevant friction model is known as the Prandtl model, which states that the shear stress is proportional to the force needed to cause plastic deformation of a given material. It is given by:

$$\tau_f = m.\tau_{máx} = m.k \tag{4}$$

Where m represents the friction factor (which is defined between frictionless conditions – and 1 – maximum friction conditions) and k is the maximum shear stress of the material. An important remark is the fact that the friction factor and the friction coefficient describe two different quantities.

As in the friction coefficient, the friction factor is dependent of service parameters, such as the temperature, speed, pressure, surrounding atmosphere and involved materials' solubility (Brown, *et al.*, 1969), which suggests that the friction coefficient varies along the contact surface. The use of a mean value of the friction coefficient is a reasonable approach to forces calculations, but can produce considerable errors when applied to determine the stress distribution on the contact interface.

Bowden and Taylor (1964) suggested that the adhesion phenomenon occurs on the contact zones between two surfaces, and the force needed to break that coupling is the friction measure. On their first studies, the maximum theoretical value for the friction coefficient was 0.2, considering that the normal pressure is independent from the shear stress. However, this value can increase significantly in different controlled surroundings. To incorporate this effect, the combined effect between the normal and shear stresses was included, and the authors presented the following formula:

$$\mu = \frac{f}{\sqrt{3(1-f^2)}} \tag{5}$$

where f is a constant that represents the shear stress on the interface (being 1 its maximum value). Bay (1985) modified this last formula, by replacing the value 3 with β_a, which represents the percentage of the surface actually capable of touching the other:

$$\mu = \frac{f}{\sqrt{\beta_a(1-f^2)}} \tag{6}$$

On the Bowden and Taylor studies, the deformation adjacent to each surface defect is considered separately. However, on cutting operations and most plastic deformation procedures the pressure on the interface is high, which increases the effective contact area between the two surfaces in question. The need to consider this effect led Wanheim and other authors, which were summarized by Bay (1985), to suggest that the friction is proportional to the normal stress for $\frac{p}{\sigma_e} < 1.5$, but for $\frac{p}{\sigma_e} > 3$ tends to a constant value:

$$\frac{\tau}{k} = m.\alpha_a \tag{7}$$

where α_a is the relation between the real and apparent contact areas.

Below, on figure 2-2, the three friction laws previously presented are shown on a normal pressure – shear stress graph. For low pressures, Coulomb and Bay models have an overlapping.

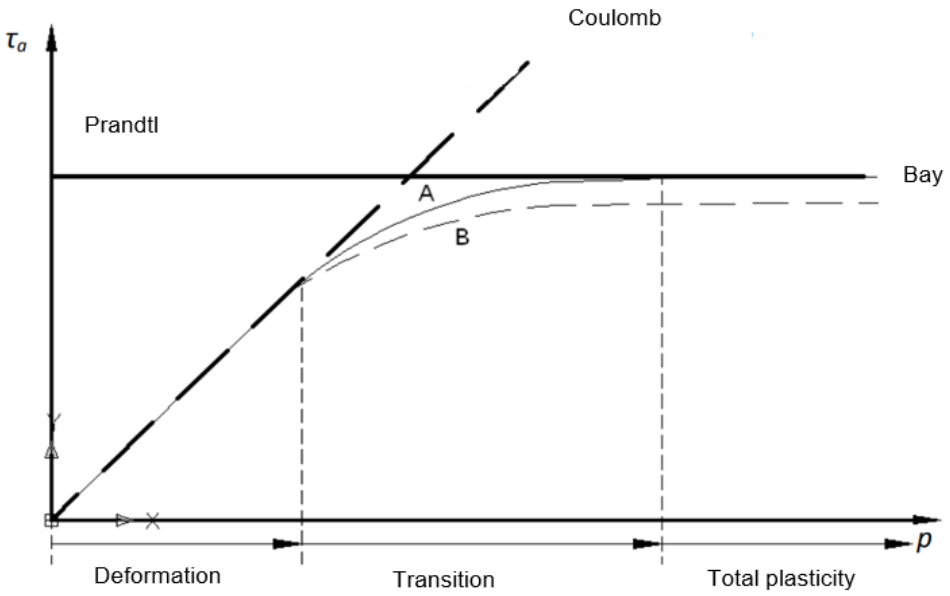

Figure 2-2. Representation of the main friction models used in engineering, showing the friction stress as a function of the normal pressure on a solid-solid interface. Two curves are generated from bay's law, a and b. Adapted from Cangundo (2009)

2.1.3. Friction Quantification Experimental Methods

Tribometers are machines that are capable of measuring friction or wear under controlled conditions. The most known experimental setups used by several investigators present in literature to quantify friction are the pin-on-disc machines, ring compression experiments and orthogonal cutting tribometers.

Pin-on-disc tests are the most common way to evaluate friction used by investigators in zones that suffer local plastic deformation and elastic deformation. On this equipment, a pin with circular or hemispheric section is pressured against a rotating disc (figure 2-3) and the friction coefficient is obtained through the relation between the tangential and normal forces, both obtained by a dynamometer (load cell).

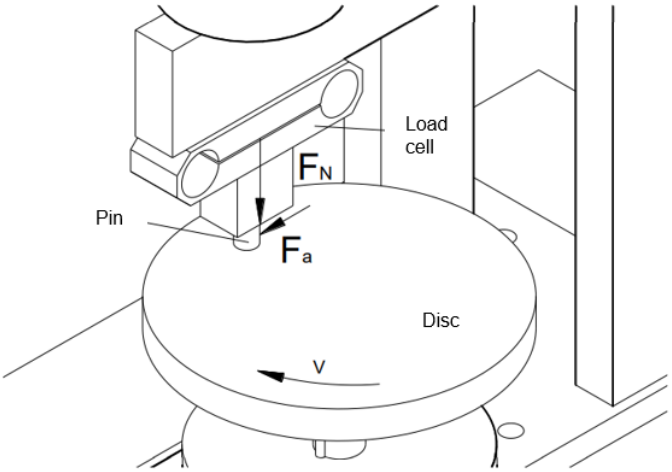

Figure 2-3. Schematic of a pin-on-disc test. Adapted from Cangundo (2009)

The thickness and diameter of the pin can be arbitrary, but they should be chosen in order to assure the system's rigidity. The superficial finish of both components (pin and disc) should coincide with the experimental conditions that are intended to be reproduced, being R_a (superficial roughness) one of the main criteria. The disc and pin's faces should be parallel, and the disc should rotate concentrically, in order to avoid undesired external forces.

The other two ways used to evaluate friction are ring compression tests, which consists of compressing a ring-shaped specimen and evaluating its degree of deformation along the process, and orthogonal cutting tests, in which the friction coefficient is obtained through the cutting and penetrative forces. Both these processes will be described in detail in the next two sections, as they are the two methods used for the present work.

2.2. Ring Compression Tests

This section is dedicated to ring compression tests. First, the fundamentals of ring compression tests will be presented. In the second subsection, recent ring compression experiments at different conditions (temperature and strain rate, respectively) will be discussed, and finally, the main equipment used will be presented.

2.2.1. Fundamentals of Ring Compression Tests

In cutting operations, as well as in metal shaping operations, friction is one of the most influential factors. One of the most widely accepted ways to evaluate the tribological behavior of a given material is performing ring compression tests, which are some of the oldest tests to characterize the tribological behavior of a given material present in literature (Male, *et al.*, 1965). This test consists of compressing a ring-shaped specimen and measuring its change in height and internal diameter throughout the process, using different tribological conditions (i.e., dry or lubricated), as represented in figure 2-4. The authors (Male, *et al.*, 1965) still suggest the usage of an outer diameter, inner diameter and height ratio of 6:3:2. The simplicity of this experiment comes from the fact that friction coefficient (μ) can be evaluated only by measuring the changes in the shape of the specimen, namely, the changes on its inner diameter and on its height. The procedure to obtain the friction coefficient present in a given process has the following steps:

1) Plot curves of height reduction (%) vs. inner diameter reduction (%) using different friction coefficients via FEM software;
2) Obtain the height reduction (%) vs. diameter reduction (%) experimental values along a ring compression experiment;
3) Overlap the experimental values with the calibration curves;
4) The friction coefficient of the calibration curve that most resembles the experimental values is the one that occurred in the ring compression test.

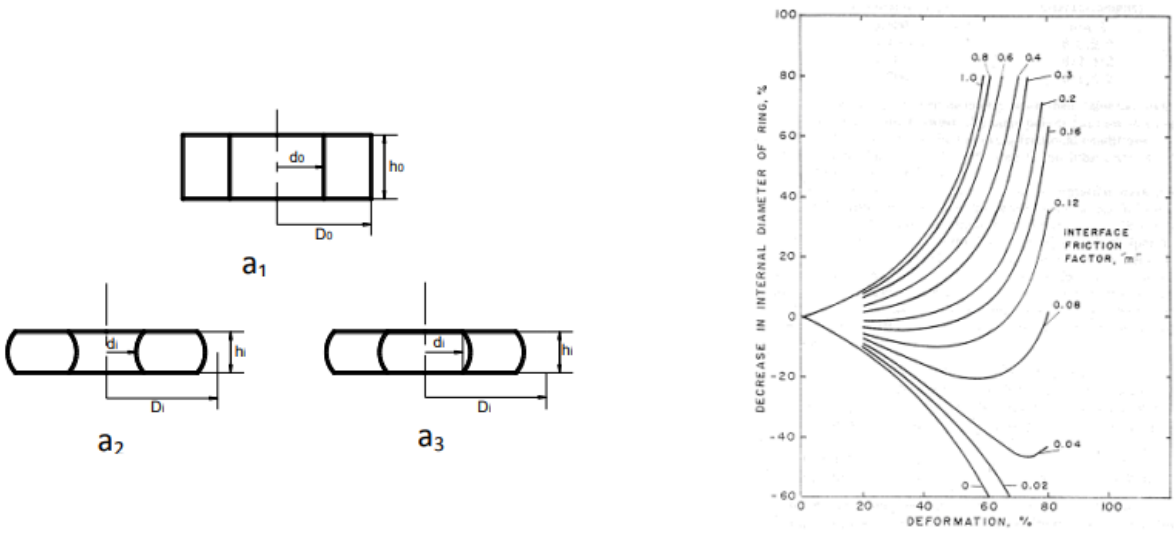

(a) **(B)**

Figure 2-4. (a) Ring deformation during compression test (Cangundo, 2009); (b) Typical calibration curves (Fletcher et al., 1998)

Dry friction is a complex process, involving inter-surface adhesion, interlocking and abrasive phenomena, which makes empirical methods a simplified and preferable approach on this topic. When the Amonton-Coulomb friction model (3) is applied alongside the Von-Mises plasticity criterion (8), we obtain a theoretical limit for the coefficient of $\mu_{máx} = 0.577$:

$$\mu = \frac{\tau_{máx}}{p} \cong \frac{k}{\sigma_y} = \frac{1}{\sqrt{3}} = 0.577 \quad (8)$$

The more deformation the material suffers (i.e. for the same height value, the lower inner diameter value), the higher the friction coefficient (Male, 1965). Besides its simplicity, the other main advantage of performing ring compression tests, comparatively to other tribological behavior characterization tests (i.e., pin-on-disc tests) is the fact that no instrumentation or electronics are needed, as the only measurements needed are the inner diameter and the height of the specimen along the experiment in order to obtain accurate friction coefficient values.

2.2.2. Temperature and Strain Rate on Ring Compression Tests

Ring compression tests are commonly performed at room temperature and slow speeds, to allow accurate measurements along the experiment. However, some metal shaping and cutting operations have high temperature and high-speed conditions, which led to the study of the influence of these phenomena on the tribological behavior of different materials by some authors. Rudkins *et al.* (1996) reported a slightly higher friction coefficient when performing ring compression tests in steel specimens at high temperatures (up to 1000ºC). The same result was archived by Shahriari *et al.* (2011) when conducting ring compression tests on Nimonic 115 superalloy using different lubricating conditions. The authors still claim that the hot ring compression test (ring compression test performed at high temperatures) is a good way to estimate the flow stress behavior and performance of a lubricant.

Other factor that has driven some attention from investigators is the strain rate effect on the ring compression test. However, studying the influence of strain rate on the friction coefficient separately can be a hard task, as the effect of temperature is present when friction at higher speeds occur. Male (1965) suggests that an increase in the press speed can provide greater lubrication efficiency when using soft or liquid lubricants. Garmong *et al.* (1977) also states that strain rate sensitive materials are more likely to changes in the friction coefficient when using different test speeds, being one of the first authors to study that matter. Other authors (Börder, 2005, Asai, *et al.,* 2017) studied the combined effects of temperature and strain-rate on the friction coefficient, and Börder (2005) studied the relative influence of these parameters on the ring compression test using steel specimens and polished compression platens, concluding that temperature is the most influential factor, followed by the type of tool coating, and finally, speed (strain rate). Asai *et al.* performed high temperature (1100 ºC) and speed (50 mm.s-1) ring compression tests and reported a slight change in the friction coefficient under those conditions.

The present dissertation focuses on ring compression tests performed on the maraging steel, both conventional and additively manufactured. However, due to the newness of the additively manufactured maraging steel, there are still few studies regarding its tribological behavior at high temperatures, and specially, at high strain rates (> 5000 s^{-1}), which is important to better understand, evaluate and optimize any process involving friction using this material. Some of the existing studies regarding the tribological characterization of this material are present in subsection 2.3.4 of the present work. Instead of ring compression tests, some authors (Sun, *et al.*, 2020, Opalinski, *et al.*, 2016) used the pin-on-disc test on this material. Sun *et al.* (2020), accordingly to previously mentioned authors (Yin, *et al.*, 2018, Vikhareva,

2020) suggests that abrasion is the main wear mechanism, but found that mild oxidational wear is the main wear mechanism in sliding speeds greater than 50 $m.s^{-1}$. The authors still found a decrease of the friction coefficient with the increase of sliding speed using the pin-on-disc test.

2.2.3. Ring Compression Tests Equipment

The equipment used to perform ring compression tests is far simpler than the ones used to perform orthogonal cutting tests, as no instrumentation is needed. The main need in these experiments is an equipment capable of compressing a specimen in very controlled conditions, at a constant speed. Consequently, the most commonly used equipment to perform ring compression tests found in literature are mechanical presses, inclusively used by the first author to conduct them (Male, 1965).

Regarding ring compression tests at different strain rates, rare cases are found in literature. One of them is the approach taken by Asai *et al*. (2018), which carried out ring compression experiments at different temperature and strain rate conditions. The authors used two different mechanical actuators to perform ring compression tests at different strain rates: a mechanical press to perform the high-speed tests, and a hydraulic press to perform low speed (quasi-static) compressions. Other authors (Hartley, *et al*, 2006), took a similar approach to the one adopted for the present work, and used a split Hopkinson pressure bar (SHPB) to perform dry and lubricated ring compression tests, as shown in figure 2-5. The authors used a servo-hydraulic test machine to perform quasi-static tests on steel, copper and aluminum ring-shaped specimens.

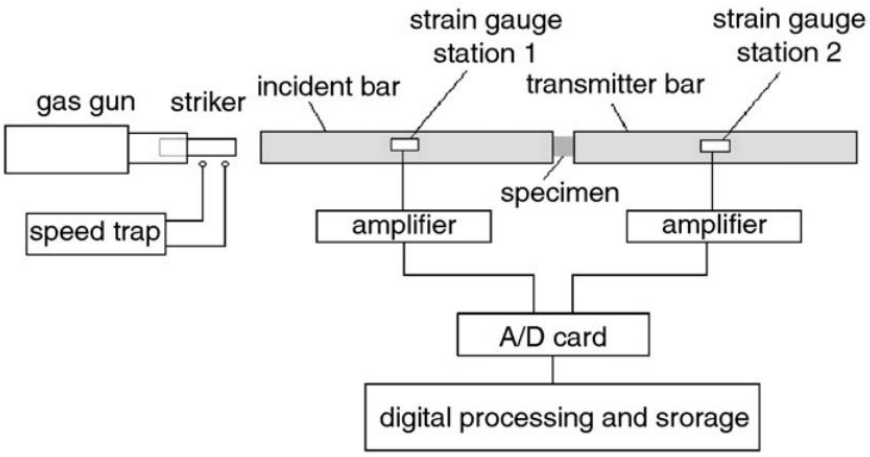

Figure 2-5 - Schematic of a typical SHPB apparatus (Hartley, et al., 2006)

However, the approach differs when higher temperature and strain rate conditions are introduced. Börder (2005) used electrical resistances to heat the compression platens (similarly to a hot forging operation), and an auxiliary furnace to heat the ring-shaped specimens. To conduct tests at different strain rates, the press speed was changed between experiments. On the other hand, Shahriari *et al.* (2011) used a furnace to heat both the compression platens and the specimen (figure 2-6). This last procedure was the one used in the present work to heat the specimens, described later in section 3.2.

(a) (b)

Figure 2-6. Two hot ring compression experimental setups: (a) The compression platens heated by electrical resistances used by Börder (2005); (b) The furnace involving the compression zone used by Shahriari (2011)

However, very few studies are present in the literature regarding the temperature and strain rate combined effect.

2.3. Orthogonal Cutting

This section is exclusively dedicated to orthogonal cutting. The classic orthogonal cutting theory, the concept of machinability and the evolution of orthogonal cutting machines along the last decades will be presented.

2.3.1. Fundamentals of Metal Cutting

The material cutting processes involved in machining operations are material removal mechanisms which are complex and hard to understand on its whole. To simplify the analysis of these processes, a plain strain, bidimensional approach is considered, as shown in figure 2-7 (Merchant, 1945). This approach is called orthogonal cutting, and assumes some postulates, including constant cutting speed (to form a continuous chip) and with perpendicular direction to the cutting edge, plane strain conditions (i.e. the specimen must be wide enough to prevent lateral deformation - $\frac{b}{e} \geq 5$), isotropic and homogeneous workpiece material and a workpiece reaction force reduction to a single resultant force applied on the cutting edge.

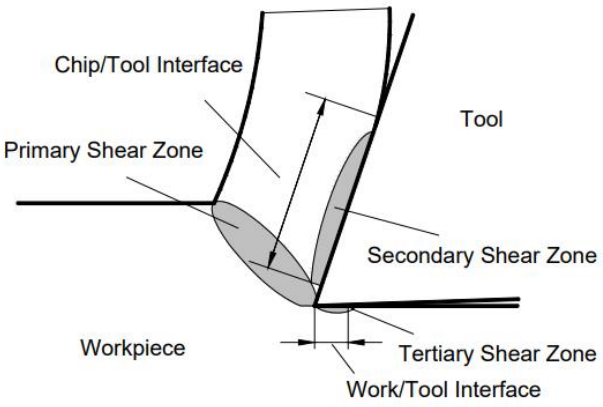

Figure 2-7.Shear zones on the orthogonal cutting process

In this process, there are three distinct cutting zones: the primary, the secondary shear zones and the sliding zone. First, the workpiece progresses towards the tool, the material is deformed, and the chip if formed on the shear plane (primary shear zone). Then, the chip starts “climbing” the rake face of the tool, giving origin to the secondary shear zone. Finally, a friction zone is developed between the tool’s clearance face and the machined surface (sliding zone).

In analytical terms, the force and velocity vectors of the orthogonal cutting take the form represented in figure 2-8.

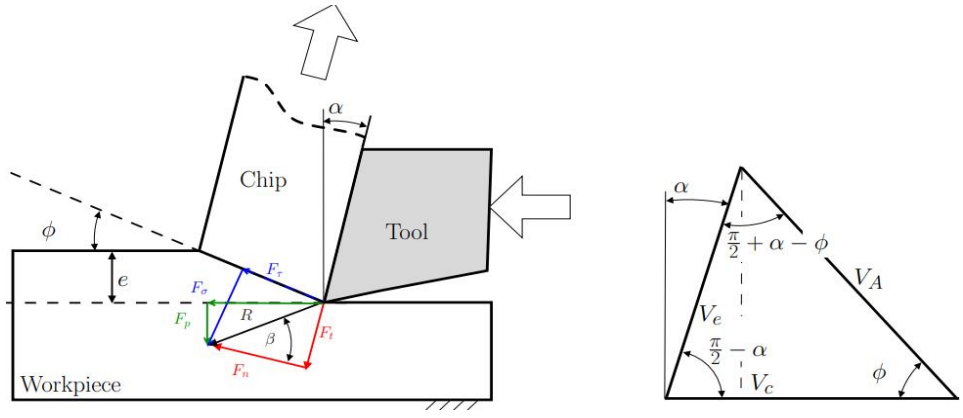

(a) (b)

Figure 2-8. (a) Force vectors; (b) Hodograph, containing the velocity vectors.

Traducing the orthogonal cutting in mathematical terms, the removed material has a known thickness, known as depth of cut, *e*. Another relevant parameter is the cut chip thickness, ***e’***. The relation between these two values is the compression ratio:

$$R_C = \frac{e'}{e} = \cot(\phi)\,.\cos(\alpha) + \sin(\alpha) \tag{9}$$

In relation to the shear plane angle, ϕ, we have:

$$\phi = \cot^{-1}\left[\frac{R_c - \sin(\alpha)}{\cos(\alpha)}\right] \tag{10}$$

To calculate the velocities involved in the process, using the incompressibility condition and the hodograph shown in figure 2-8, we obtain:

$$V_e = \frac{V_c}{R_C} \tag{11}$$

$$V_A = V_c\left(\frac{\cos(\alpha)}{\cos(\phi-\alpha)}\right) \tag{12}$$

To compute the forces involved in orthogonal cutting, using the forces diagram in figure 2-8 and trigonometric relations, we have:

Shear plane

$$F_\tau = F_C \,.\cos(\phi) - F_p.\sin(\phi) \tag{13}$$

$$F_\sigma = F_C \,.\sin(\phi) + F_P \,.\cos(\phi) \tag{14}$$

Rake face

$$F_N = F_C \,.\cos(\alpha) - F_p \,.\sin(\alpha) = R.\cos(\beta) \tag{15}$$

$$F_T = F_C \,.\sin(\alpha) + F_P \,.\cos(\alpha) = R \,.\sin(\beta) \tag{16}$$

Main forces

$$F_C = R \,.\cos(\beta - \alpha) \tag{17}$$

$$F_p = R \,.\sin(\beta - \alpha) \tag{18}$$

where β is the friction angle and R is the resultant force. This angle is calculated using the friction coefficient:

$$\beta - \alpha = \tan^{-1}\mu \tag{19}$$

$$\mu = \frac{F_T}{F_N} \tag{20}$$

Its value was obtained by (20) for the present work. However, when the friction coefficient is not known, Lee & Shaffer, using the slip line theory and the Mohr circle, propose the following expression for the friction angle:

$$\beta = \frac{\pi}{4} + \alpha - \phi \tag{21}$$

With this angle, the contact length between the chip and the rake face of the tool, and the strain rate of the process can be obtained:

$$l_{ct} = e.\left(\frac{sen(\beta + \phi - \alpha)}{sen(\phi).cos(\beta)}\right) \tag{22}$$

$$\dot{\varepsilon} = \frac{cos(\alpha)}{cos(\phi - \alpha)}.\frac{V_c}{\Delta y} \tag{23}$$

where Δy is the thickness of the primary shear zone. Finally, there is another relevant parameter, which is the specific cutting pressure:

$$K_s = \frac{F_c}{A_0} \tag{24}$$

where A_0 is the cross-sectional area of the undeformed chip (i.e. $A_0 = e.b$). This is a parameter of high relevancy to determine the efficiency of a cutting process.

2.3.2. Orthogonal Cutting Apparatus

The first machine tools dedicated to orthogonal cutting found in literature were developed during the industrial revolution (XIX century) due to the need of obtaining plane surfaces. One of these machines is the steam-arm shaper developed by Naysmith in 1836 (Steeds, 1969), in which the tool was mounted to a ram driven by a connecting rod, as shown in figure 2-9. This machine was often used to make notches or holes in mechanical components, such as keyways or gears. However, as the cutting tool holder is connected to the connecting rod, the tool speed is not constant: it increases in the beginning, and it starts decreasing gradually to zero throughout the cutting process.

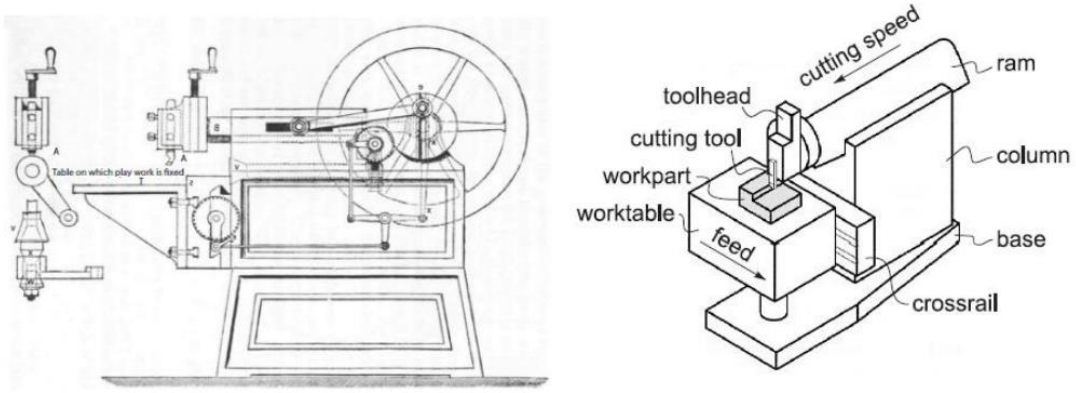

(a) (b)

Figure 2-9. (a) Naysmith's steam-arm shaper (Steeds, 1969); (b) Simplified scheme.

However, the development of orthogonal cutting machines with investigation purposes (to study specifically machining phenomena) has been increasing over the last decades, as a significant amount of information about machining processes can be gathered in this process, besides the experimental setups used by the authors referred in the next paragraphs being relatively simple. One of those is the experimental apparatus developed by Akiyama *et al.* (1974), in which a hydraulic piston pushed a workpiece through an upper, a lower and two side constraining plates against the cutting tool edge, as shown in figure 2-10

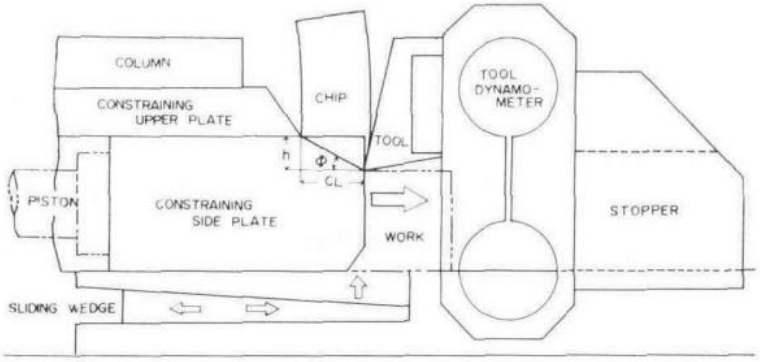

Figure 2-10. 2D scheme of the orthogonal cutting machine used by Atknins et al. (1974)

The workpiece materials used are pure lead (99.98%) and a Pb-Sn alloy (91.5% Pb and 8.5 Sn), and the cutting tools used are made of 10 % Co type high speed steel, finish ground to geometries of σ = 5º clearance angle and α = 10º, 20º, 30º and 40º rake angles. The side plates have the purpose of constraining the material to orthogonal cutting conditions. This machine can perform tests at very low speeds (0.1 $m.min^{-1}$) to minimize the thermal effects on chip formation. To measure forces and chip thickness, hexagonal type ring dynamometers and a micrometer were used, respectively. This apparatus was used to study the minimum energy dissipation condition in orthogonal cutting, as well as to compare with the results obtained from Merchant's equation.

In the following years, some high speed orthogonal cutting machines were also developed, such as the ones used by Özel & Altan (2000) and Kandibanda (2008). Both of them have a very similar way of functioning: the workpiece is fixed to a rotating mandrel, a cutting tool insert is mounted onto a tool-holder, and the metal cutting if performed through the feed movement of the worktable, to which the tool-holder is attached, as represented in figure 2-11. This design is still largely used nowadays in high -speed orthogonal cutting tests.

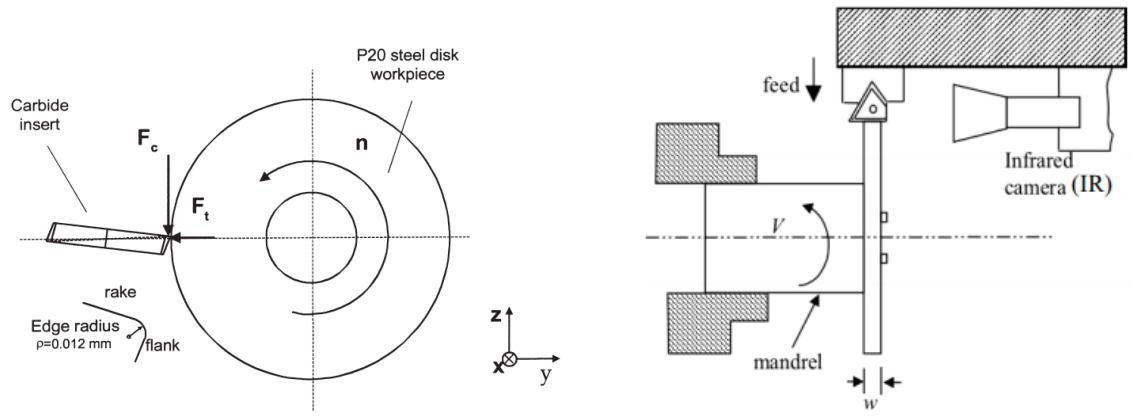

(a) (b)

Figure 2-11. 2D schemes of the experimental apparatus used by (a) Özel & Altan (2000; (b) Kandibanda (2008).

The machine used by Özel & Altan (2000) allows cutting speeds as high as 550 $m.min^{-1}$, and feed rates between 0.025 and 0.1 $mm.rev^{-1}$ were used. However, sudden tool failure occurred at 550 $m.min^{-1}$ cutting speed with 0.075 and 0.1 $mm.rev^{-1}$ feed rates. The authors used this testing machine to obtain the cutting forces and chip geometry of P20 steel, to determine flow stress at high deformation rates and temperatures that are encountered in the cutting zone, as well as to study the friction phenomena at the chip–tool interface.

However, while also operating at high speeds, Kandibanda (2008) used lower cutting speeds (175 $m.min^{-1}$) and a slightly more restrictive feed rate range (between 0.05 and 0.4 $mm.rev^{-1}$). The author also used a Kistler 9121 three component tool dynamometer to measure forces, and a FLIR Systems ThermaCam PM695 infrared camera to measure temperature on the tool-chip interface. This experimental apparatus was developed to study the effect of edge radius on cutting forces, temperature

across various points on the tool, micro-hardness, microstructure and residual stresses on AISI 1045 steel. Both Kandibanda (2008) and Özel (2000) used an uncoated carbide insert as cutting tool.

With the growing progress in technology, some high precision orthogonal cutting machines were recently developed, such as the one developed and used by Frometin *et al.* (2016). In this machine, there are two adjustable axes. The x-axis supports the work piece and imposes to the table its back and forth linear motion with the help of a custom designed hydrostatic guideway and of an electric linear motor, as shown in figure 2-12.

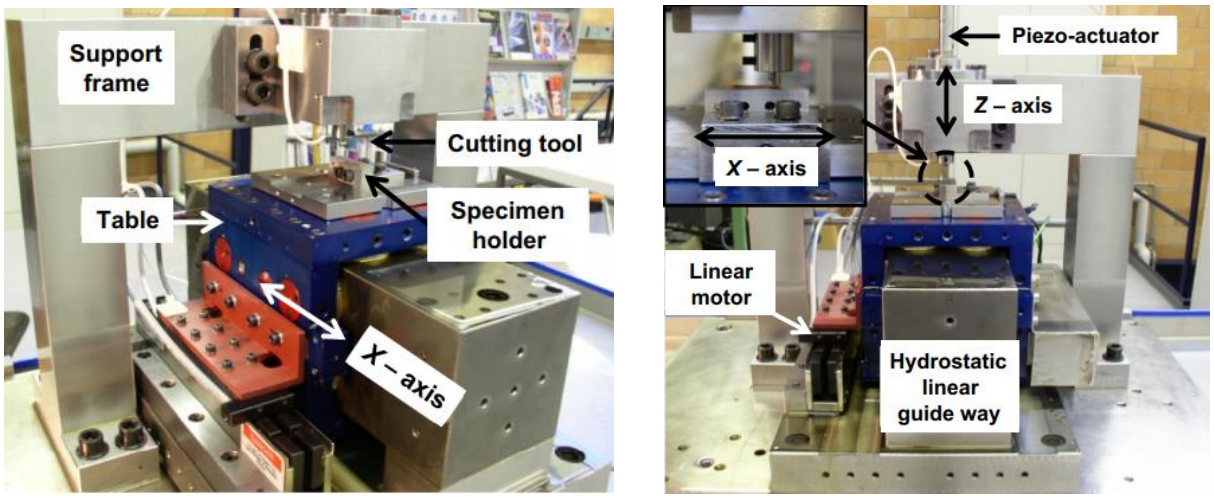

Figure 2-12. Orthogonal cutting machine developed by Frometin et al. (2016).

The z-axis holds the tool and has both a coarse manual adjustment over a range of 25 mm and a fine feedback-controlled positioning of 0 to 80 µm. The linear movement of this axis is imposed by a piezoelectric actuator and guided by a set of two thin flexible diaphragms. The maximum bidirectional stroke (back and forth stroke) of the machine is 100 mm, the steady state speed range is 0.0024 to 60 $m.min^{-1}$, and it allows to perform orthogonal cutting tests with accuracy better than 1 µm.

To perform force measurements, the authors used a Kistler 9217 piezoelectric force sensor for the x-axis, which measures the cutting force, and a Kistler 9215 piezoelectric force sensor for the z axis, which measures the thrust force. To position measurements, an optical scale (Heidenhain LIP 401) measures the x-position of the workpiece table with micrometer resolution and provides the feedback signal for controlling the linear motor. The position of the z-axis is measured by means of an Eddy current sensor (Eddy NCDT 3700). To determine the true cut thickness, a Keyence LC-2400 W with LC-2430 head laser profiler was used (the true cut thickness is the difference between a laser measurement before cutting and one after). The author used this machine to perform cutting tests on 316L stainless steel and 9 % Zn brass using a tungsten carbide tool and cutting depths as low as 5 µm.

Due to the emergence of new difficult to machine materials in the last years and decades, there is also a growing number of orthogonal cutting studies regarding them. One of these is the work conducted by Lopresto *et al.* (2017) to study orthogonal cutting on unidirectional carbon and glass fiber reinforced plastics at high and low speeds. To perform high speed tests, the authors used a rotary mandrel with

the specimen and the feed movement of the worktable to which the tool is attached, resembling the systems used by Özel & Altan (2000) and Kandibanda (2008). On the other hand, to conduct low speed tests (0.01 m.min^{-1}), a fixe axis machining centre was used. During the tests, the fiber reinforced plastic workpiece and the HSS tool were fixed to the table and the stationary overarm of a milling machine, respectively. The relative tool-material motion was accomplished by the table feed, as shown in figure 2-13.

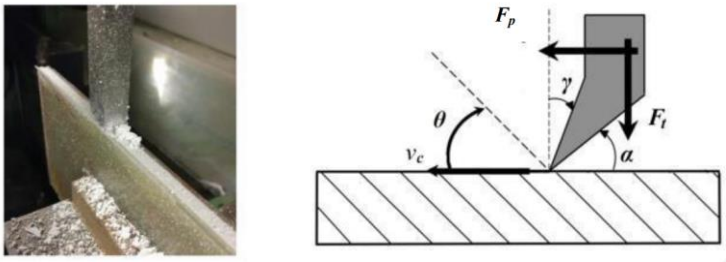

(a) **(B)**

Figure 2-13. (a) Orthogonal cutting machine developed by Lopresto et al. (2017); (b) 2D scheme.

During all the tests in the above presented conditions, principal cutting and thrust forces were measured by a Kistler 9257A three channels piezoelectric dynamometer and Kistler 5008 charge amplifiers. Using this experimental apparatus, the authors could perform orthogonal cutting tests varying the rake angle (HSS tools with five different geometries were adopted), cut depth and fiber orientation of the composite made workpiece, studying its influence on the chip formation mechanisms (especially the fiber orientation influence).

During the last years, several orthogonal cutting machines were developed inside IST, where the present work was carried out. Santos (2005) studied the influence of the main cutting parameters on the chip geometry, in orthogonal cutting conditions. The material used was pure lead (99.9 %) with a density of 11.35 g/mm^3, hardness of 1.5 Mohs and melting point of 327.46ºC. The experimental apparatus used is indicated in figure 2-14. A hydraulic press with a maximum force of 500 kN was used to create very low-speed conditions (adjustable up to 6 m.min^{-1}). The press has four columns, a power of 44 kW and a total stroke of 300 mm. To perform orthogonal cutting tests, Santos (2005) attached a cutting tool to the press piston and attached the specimen to the worktable, which can be adjusted by a digital micrometer.

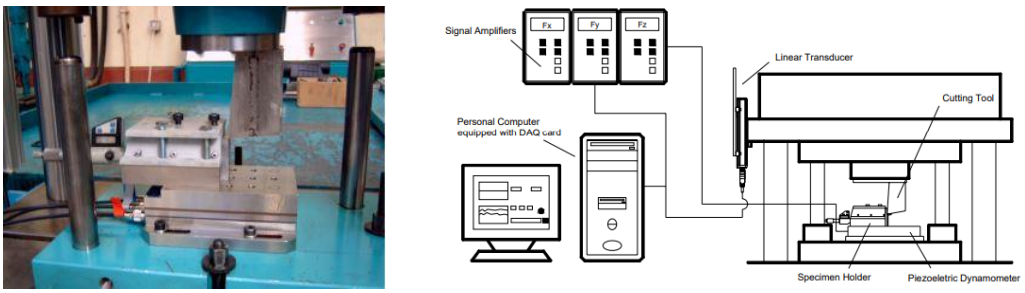

(a) (b)

Figure 2-14. (a) Experimental apparatus developed by Santos (2005); (b) 2D scheme.

The hydraulic press is controlled by position numerical control, which executes automatically the programs defined by the user. In this work, there were also used cutting tools with different rake angles (-10º, -5º, 9º, 5º and 10º). To measure the tool displacement, a Balluf BTL5.-A11-M0500-P-S32 linear position sensor was used. To measure the cutting forces, a piezoelectric load cell Kistler® 9257B was used. It has a reading interval of ±10 kN, a 7.5 V/pC sensitivity on the x-channel and 3.5 V/pC on the y and z-channels. The signal passes through a Kistler® type5011B amplifier before entering the DAQ (National Instruments®, model NI-PCI-6070E, 16 1.25 MS/s analogic channels, 12 bits resolution, and a voltage interval of ±10). To connect this system to the computer, a CB-68LP terminal block was used, with 68 terminals with 68 pins, and a connecting cable R6868 also with 68 pins. The computer receives the data and exports them to a *.txt* file, using the software *LabView*. The file is then analyzed and processed using Microsoft® Excel.

Later, both Cristino (2007) and Carrilho (2007) used this same experimental apparatus with no substantial changes. Cristino (2007) studied the metal cutting process oriented to the evaluation of analytical solutions, and Carrilho (2005) analyzed the friction force throughout the rake face of the cutting tool.

Cangundo (2009) studied the tribological condition in the metal cutting process at low speed (up to 1 $m.min^{-1}$). To perform the tests, a 3 axis CNC TRIAC milling machine was used to move the copper and AISI 316L specimens relatively to a fixed cutting tool with fixed angles (α=0° and σ=5°). Both the load cell and the amplifier are the ones used by Santos (2005). The table movement was programmed through G code. Cangungo (2009) inclusively developed a pin-on-disc apparatus to compare the obtained results to the ones obtained in orthogonal cutting experiments.

Pereira (2009) analyzed the influence of various parameters in the orthogonal metal cutting process in pure lead (99.7%). The DMG 63V machining available at *Laboratório de Tecnologia Mecânica* was used. This machine can produce higher cutting speeds comparatively to the previous ones (from 0.6 $m.min^{-1}$ to 30 $m.min^{-1}$), but has similar instrumentation equipment (same DAQ, load cell and amplifier). Later, Cordeiro (2010) also used this machine to compare aluminum (99.5 %) cutting with finite element simulations.

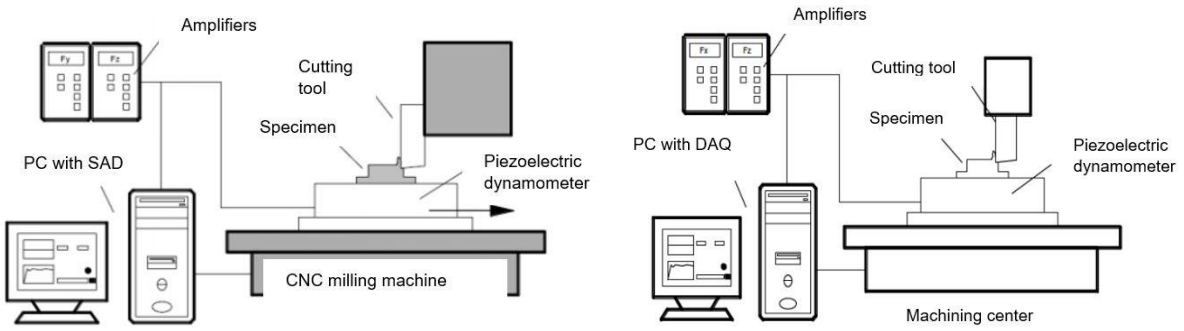

(a) (b)

Figure 2-15. 2D schemes of the experimental apparatus developed by (a) Cristino (2007); (b) Cangundo (2009).

Up to now, all the machines developed can only perform orthogonal cutting tests under low speed. Fernandes (2017) developed the first experimental apparatus to perform metal cutting at high speed (200 $m.min^{-1}$), by using an electromagnetic actuator. It produces these speeds through the discharge of five condensers (which can store voltages as high as 400 Volts). This machine was developed to study the importance of oxygen in the tribological behavior of the pure lead and AA1050 aluminum cutting.

The apparatus itself consists of a closed chamber (to control the metal cutting atmosphere) that contains the machine components, such as the specimen fixation system, the load cell, the position sensor and a guide supported by two ball guide rails. This machine has a closed structure, and three holes to inject the gas. All of this can be observed in figure 2-16.

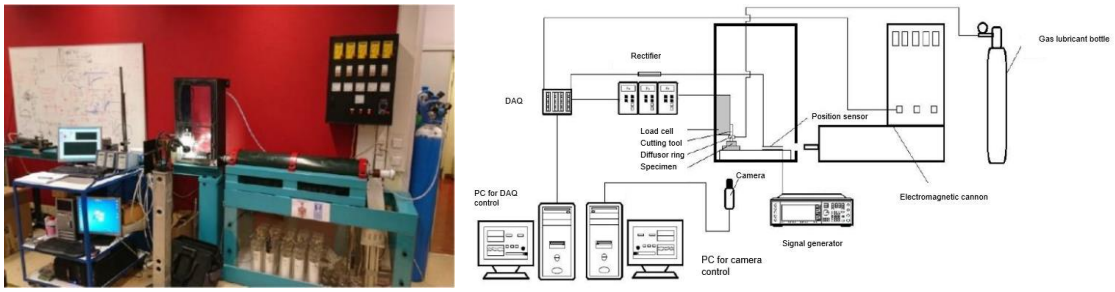

(a) (b)

Figure 2-16. (a) Experimental apparatus developed by Fernandes (2017); (b) 2D scheme.

This apparatus contains a TTi® TG120 analogic signal generator between 0 and 20 V, a Basler® acA2000-340km high speed camera (which can capture up to 6000 frames per second and has a 2 MP resolution) and an induction-based position sensor. The load cell and the amplifier used were the same used in previous works in IST.

Besides the innovation of this apparatus, there were some inconsistent results due to the lack of structural rigidity when higher loads (and consequently, higher strain rates and dynamic cutting conditions) were applied.

To improve structural rigidity, while maintaining high cutting speeds, Andrade (2019) developed an experimental apparatus with 8 steel plates (to which the cutting tool is attached). This assembly can be seen in figure 2-17 (a). The high-speed tests were performed using the same electromagnetic actuator, condensers and linear guide used by Fernandes (2017). However, Andrade (2019) added one more ball guide rail to offer more stability to the guide that holds the specimen.

(a) (b) (c)

Figure 2-17. (a) Experimental apparatus developed by Andrade (2019); (b) Specimen fixation system; (c) tool fixation system.

To attach the specimen to the linear guide, a mechanical fixation device was developed in order to enhance structural stability (shown in figure 2-17 (b), in which the Kistler® system used to attach the cutting tool to the load cell) is also represented. To measure the forces values, a piezoelectric Kistler® 9257A load cell was used, but only two of the its three channels were operated (to measure the penetration and cutting forces). To connect the load cell to the DAQ, two channels of a Kistler® Type 5007 amplifier were used. Finally, to measure the displacement of the specimen while being cut, the induction-based sensor that Fernandes (2017) developed was used, which was powered by a FeelTech® FY3200S Dual Channel signal generator and connected to a rectifier, before entering the DAQ. All this system can be observed in figure 2-18.

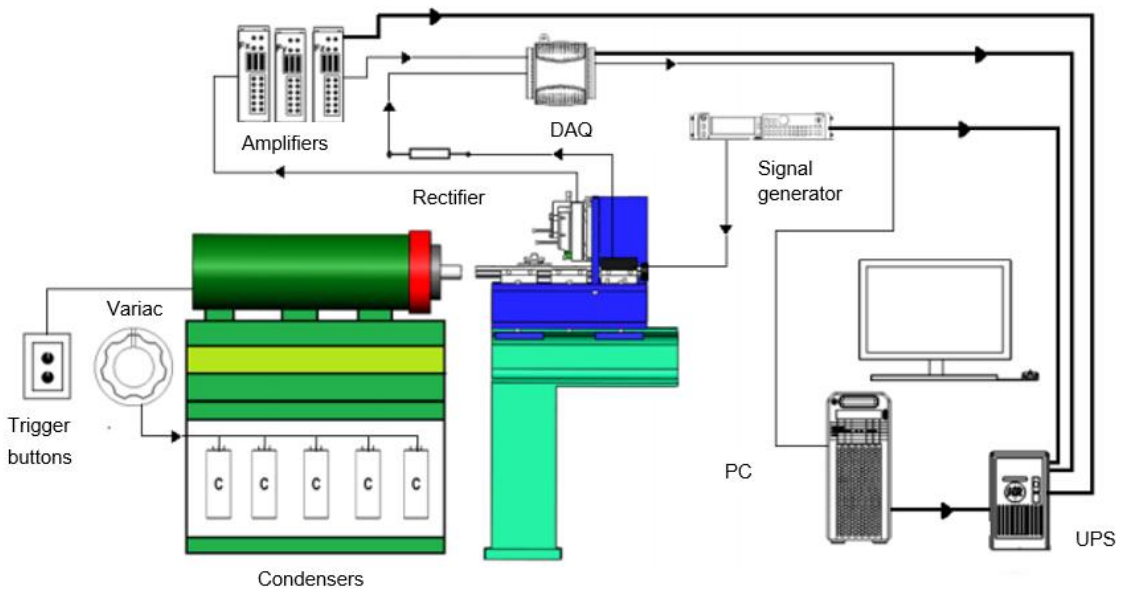

Figure 2-18. 2D scheme of the experimental apparatus developed by Andrade (2019).

Andrade (2019) used this machine to study the influence of glycerin in AA1050 aluminum in a big speed range (0 – 200 $m.min^{-1}$). In the low-speed tests, the specimen was pushed manually against the tool at a constant speed with the help of a lever.

Besides the higher rigidity obtained, the author refers some problems with the cutting tool used and the specimen fixation device, as well as the specimen material itself (its extremely ductile behavior made a

rigorous orthogonal cutting analysis difficult, due to the lack of chip formation mechanisms). Other problem stated is the fact that the electromagnetic actuator does not provide a low cutting speed for quasi-static conditions. The author also suggests welding the plates that hold the fixation tool, as well as to grind the specimen before cutting it in future works.

2.4. Materials Obtained by Additive Manufacturing

Additive manufacturing (or 3D-printing) has attracted attention regarding future production and repair of parts, as it allows components with complex geometries that cannot be obtained through the conventional subtractive manufacturing processes (Peng, *et al.*, 2018). More recently, 3D-printing of metal parts have raised expectations on the aerospace industry. The most common ways these components are manufactured are Selective Laser Melting (SLM), Electron Beam Melting (EBM), Direct Energy Deposition (DED) or Binder Jetting, by using metal powders as feedstock (Fredriksson, 2019). The partitioning of additive manufacturing (AM) technologies into powder-bed and deposition technologies can be observed in figure 2-19.

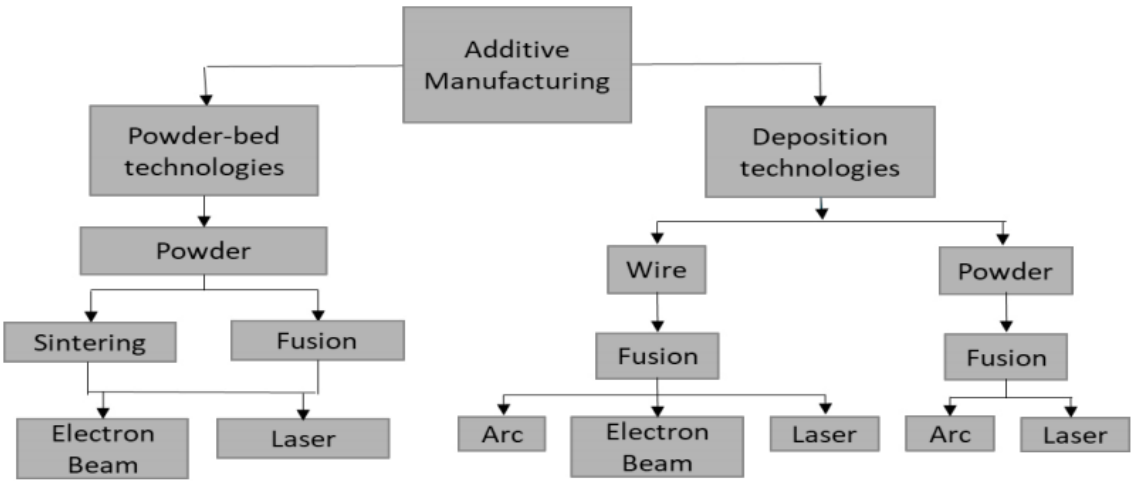

Figure 2-19. Schematic overview of some key additive manufacturing technologies (Fredriksson, 2019).

Parts obtained by AM can require post-machining operations to meet the intended surface finish and dimensional accuracy. However, there are some drawbacks when machining these parts, such as powder adhesion phenomena and poor surface roughness inherent to balling effect (Peng, *et al.,* 2018), which makes them harder to machine, comparing to the same material at conventional state, as stated by many investigators. Montevecchi *et al.* (2016) noticed significantly higher cutting forces in AISI H13 parts obtained by AM, comparing to the conventional AISI H13. The same phenomenon was observed by Polishetty *et al.* (2017) when machining Ti-6Al-4V obtained by AM (Selective Laser Melting), comparing to the conventional alloy, using tungsten carbide tools and cutting speeds between 45 and 180 $m.min^{-1}$. The authors still observed a lower surface roughness in the same material, when obtained by AM, and for all cutting speeds, due to the high hardness and brittle characteristics of SLM Ti-6Al-4V. Despite the investigation carried out, an in-depth investigation about how this material's microstructure affects its bad machinability is suggested. However, Bonaiti *et al.* (2017) state that the resultant cutting forces are lower in Ti-6Al-4V obtained by direct energy deposition, despite their higher hardness (due

to their finer microstructure), comparatively to the conventional alloy. The authors also claim that higher roughness values were observed with the increase of feed rate and depth of cut. In terms of the additive manufacturing process of the titanium alloy itself, the authors found an increase in hardness and a decrease in porosity with the increase of the laser power, thus improving the overall integrity of the material samples. Optimizing the deposition process considering the machinability as a functional material characteristic is also suggested as a future work. As titanium parts obtained by additive manufacturing are very recent techniques, there is also a lack of studies comparing the machinability of parts obtained by the different AM techniques.

Other authors studied other aspects of materials obtained by AM machining. Segebade *et al.* (2019) observed differences in the cutting forces and chip geometry when varying the cutting direction, due to the anisotropy present in AlSi10Mg specimens obtained by AM, and Heigel *et al.* (2018) observed contraction after machining AISI stainless steel tubes obtained by AM (laser powder bed fusion), possibly due to the compressive stresses induced during the additive manufacturing process. The authors still stated the need of additional investigations to better understand the complex interaction between additive and subtractive manufacturing processes.

2.4.1. The Maraging Steel

An interesting material which is starting to be used to create parts obtained by AM is the maraging steel, commonly known for its higher mechanical resistance. This steel is commonly obtained through SLM (Selective Laser Melting), which gives the additive manufactured maraging parts high mechanical strength and (seemingly) good machinability. Maraging 300 parts obtained by AM also present a cellular microstructure and a ductile-type fracture mechanism consisting in void nucleation, growth, and their coalescence (Casati *et* al., 2016). Some authors studied the effects of ageing on maraging steels, which forms strengthening precipitates. Some of these effects include an increase in tensile performances and hardness, but a decrease in toughness (Casati *et al*., 2016, Simson et al., 2019). Other authors (Ansell *et al*., 2020) also studied the effect of the printing orientation (vertical, 45º and horizontal, relative to the print plate), and found higher ultimate tensile strength in vertical and 45º specimens, but higher tensile properties than conventional maraging steel in all specimens, especially the specimens printed with vertical orientation. However, the authors still state that ductility and toughness of maraging parts obtained by AM are lower than conventional material ones, and producing maraging 300 parts using SLM has some major drawbacks, including high costs of production, size limitations, long production times (Kučerová *et al.,* 2020) and the need to prior post-processing machining.

On the other hand, conventional maraging steel (obtained by conventional processes) has a microstructure change, when aged. Lohmann *et al.* (2019) found that maraging 300 steel, when aged at 480ºC, 580ºC and 650ºC, produces a rearrangement in the martensite phase, as well as a common occurrence in maraging steels: austenite reversion, which gives the material more mechanical strength. The extent of these phenomena depends on the time and temperature of the heat treatment.

Maraging steels obtained by conventional manufacturing processes are also known for their bad machinability. However, Bhukya *et al.* (2014) have found the optimal set of cutting parameters (cutting

speed, feed and depth of cut) that produce minimum cutting force and minimum surface roughness, thus finding the parameters that allow the best machinability. A cutting speed of 45 $m.min^{-1}$, feed of 0.051 $mm.rev^{-1}$ and a depth of cut of 0.5 mm are optimal parameters for minimal cutting force, and a cutting speed of 75 $m.min^{-1}$, feed of 0.094 $mm.rev^{-1}$ and depth of cut of 1.5 mm are the best values for minimum surface roughness. The authors still found that surface roughness values are lower at lower speeds, and at higher speeds the Maraging surface quality seems to deteriorate.

There are few studies regarding the tribological characterization of this material, both conventional and AM due to its newness. Still, Vikhareva (2020) claims that abrasion and galling are the main wear mechanisms at high temperatures in maraging steel obtained by SLM, when analyzing forging at high temperatures. Yin *et al.* (2018) also found a decrease in the wear rate on maraging steel obtained by SLM when the temperature increases. The authors still suggest that abrasion is the main wear mechanism until 490ºC, where adhesion tribofilm starts to be the dominant wear mechanism.

3. Experimental Development

This chapter is mostly dedicated to the orthogonal cutting tribometer developed through the course of the present dissertation, which was used to perform the cutting tests described in chapter 4. The machine will be described in detail, including all its components, functions and capabilities. Secondly, the ring compression machine and experimental methods used will be also presented. Finally, in the last section, the full orthogonal cutting and ring compression plan of experiments will be shown.

3.1. Orthogonal Cutting Tribometer

The orthogonal cutting tribometer developed for the present work is situated in the *M3* laboratory, at *Secção de Tecnologia Mecânica e Gestão Industrial*, in IST. Its development has the purpose of performing orthogonal cutting tests at low speed conditions. The machine is composed of two parts: an experimental orthogonal cutting apparatus, where many of the parts used by Andrade (2019) were chosen, where the cutting process occurs, and a part that contains a pneumatic cylinder, which will supply the necessary power to the process and cutting speeds up to 4 $m.min^{-1}$. The cylinder is connected to a structure of five CK45 steel plates, which are fixed to two linear guides by 4 M12 screws. The linear guides are held and stabilized by two ball guide rails (STAR – Ball Rail® System Runner Blocks 1653 – Size 65), which allow the cylinder to move in the horizontal axis (in order to create space for a future assembly of another actuator). When activated, the cylinder pushes the linear guide (to which the specimen is attached), forcing the specimen against the tool and therefore making the cutting process occur. The linear guide is held and stabilized by three ball guide rails (STAR – Ball Rail® System Runner Blocks 1653 – Size 45), which are connected to a structure consisting of six CK45 steel plates (to which the cutting tool is also connected). Some of these components are the same used by Andrade (2019).

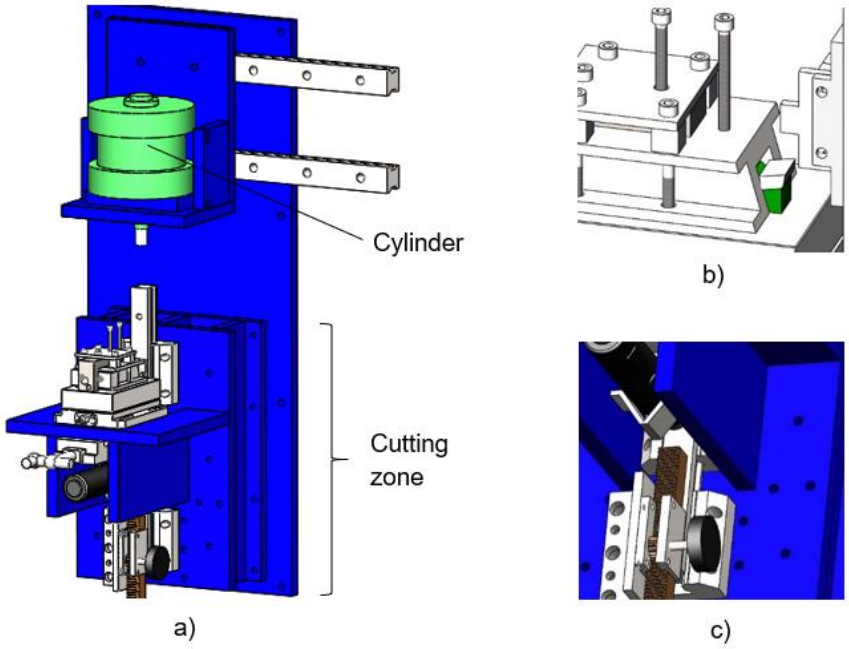

Figure 3-1. CAD model of the: (a) Orthogonal cutting tribometer; (b) Detail of the cutting tool holder and cutting tool; (c) Detail of the grinding zone, on the bottom of the cutting zone of the machine

The depth of cut can be adjusted by a micrometric screw. When the depth of cut is fixed, the tool holder can be tightened by friction using screws. The specimen fixation system was also the one used by Andrade (2019). It is attached to the linear guide by two M8 screws, and it tightens the specimen through two horizontal screws and one vertical screw, in order to restrict its movement as best as possible. The machine developed is also equipped with a zone that allows grinding the specimen before cutting (to remove any hardened layers, impurities or surface unevenness that can affect the cutting tests results), as suggested by Andrade (2019). The specimen can be moved manually between the cutting and grinding zones by a rack pinion mechanism, as represented in figure 3-1. All this system is connected to a 1000 x 400 mm CK45 plate by 12 M8 screws and 16 M10 screws. The plate is then connected to a wall by chemical bushing with 8 M10 screws.

During the cutting process, a load cell measures the forces involved (cutting force and penetration force) and a linear potentiometric position sensor measures the displacement of the specimen during the operation. This information is then read by a data acquisition card (DAQ), through *LabView* software, and the corresponding values are shown in a computer screen. Except for the amplifier, all the electronic components are powered by an UPS. The full system developed is represented in figure 3-2, and the developed machine is shown in figure 3-3.

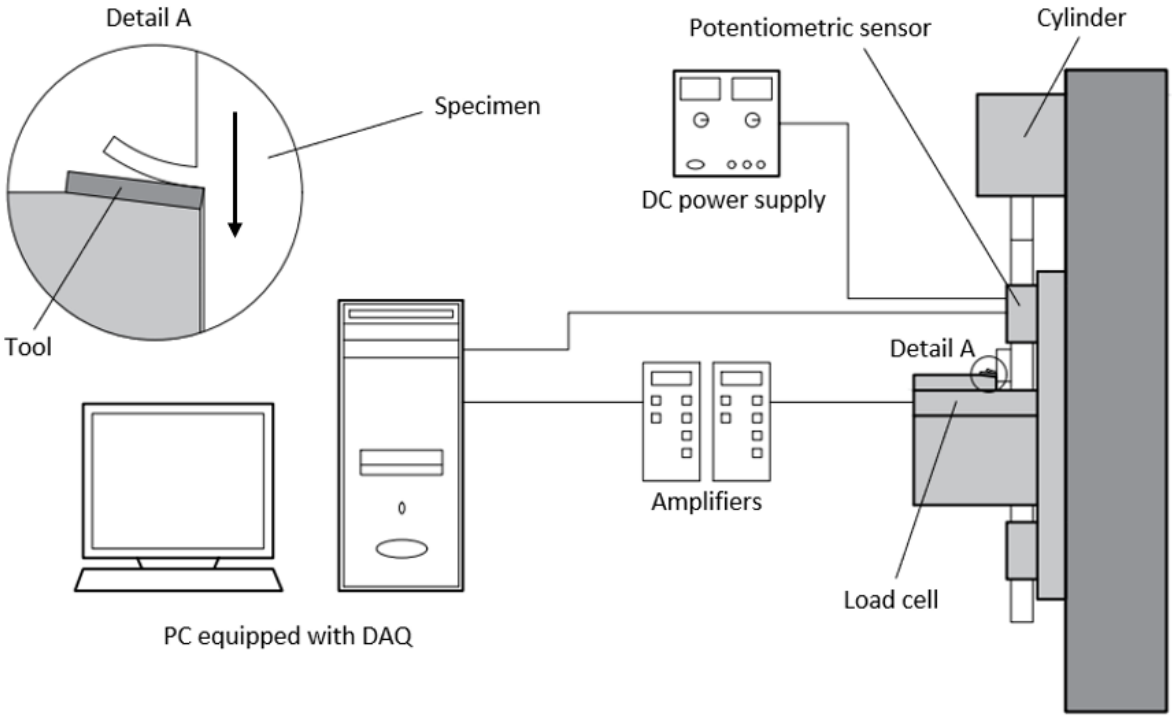

Figure 3-2 – Full schematic of the machine and its electronic components

(a) (b)

Figure 3-3. (a) Orthogonal cutting tribometer; (b) Electronic equipment used to supply and receive the data from the sensors

To measure the cutting forces and the displacement along the process, in order to obtain the friction coefficient, two sensors were used. To measure the forces, a Kistler® 9257A piezoelectric load cell was used (the same one used by Andrade, 2019). This load cell has a measurement range of +/- 5000N on the x and y-directions, and +/- 10000N on the z-direction. To adjust its output signal to the DAQ's reading capacity, a Kistler® Type 5007 amplifier was chosen, calibrated with the same parameters used by Andrade (2019) – sensitivities of 7,5 pC/N on the x and y directions, and 7,5 pC/N on the z-direction. A TC = LONG time constant and an S = 1000 amplification factor were also used. Therefore, the same calibration curves obtained by Andrade (2019) to convert the output voltage to Newton were also used:

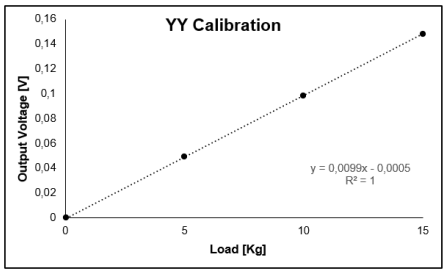

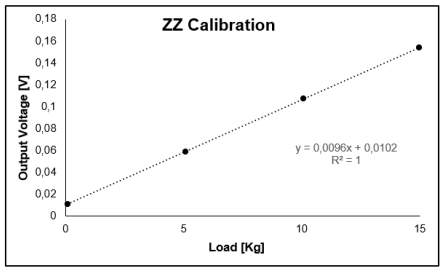

(a) (b) (c)

Figure 3-4 – (a) Kistler load cell used (the same one used by Andrade, 2019); (b) Calibration curve on the yy direction; (c) Calibration curve on the zz direction

To measure the displacement of the specimen along the process, a linear potentiometric displacement sensor was placed on the cutting zone (the specimen fixation system pushes the sensor's tab along the

process). A DC power supply was used to feed the sensor at 5V. The sensor is approximately linear, as shown in figure 3-6 below:

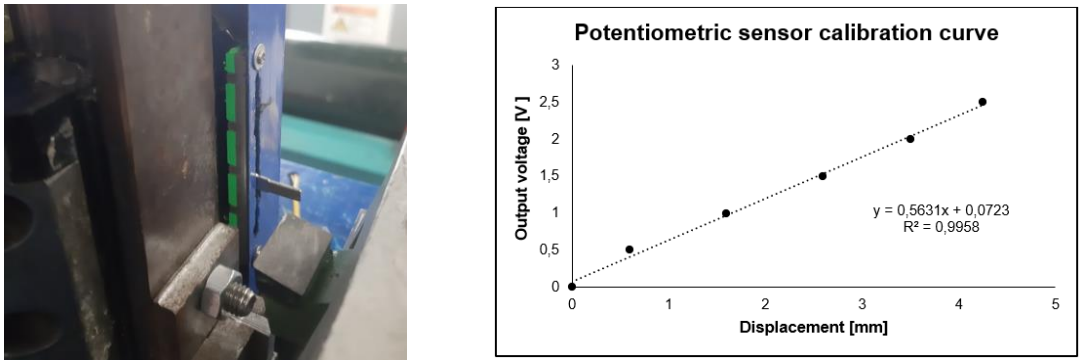

(a) (b)

Figure 3-5 – (a) Potentiometric sensor; (b) calibration curve of the sensor

In order to check if the machine is capable of performing orthogonal cutting tests, a cutting test on a AA1050 aluminum specimen (the same used by Andrade, 2019) was performed, using a 0.02 mm cut depth and 3 $mm.s^{-1}$ test speed. The resulting cutting forces are shown in figure 3-6.

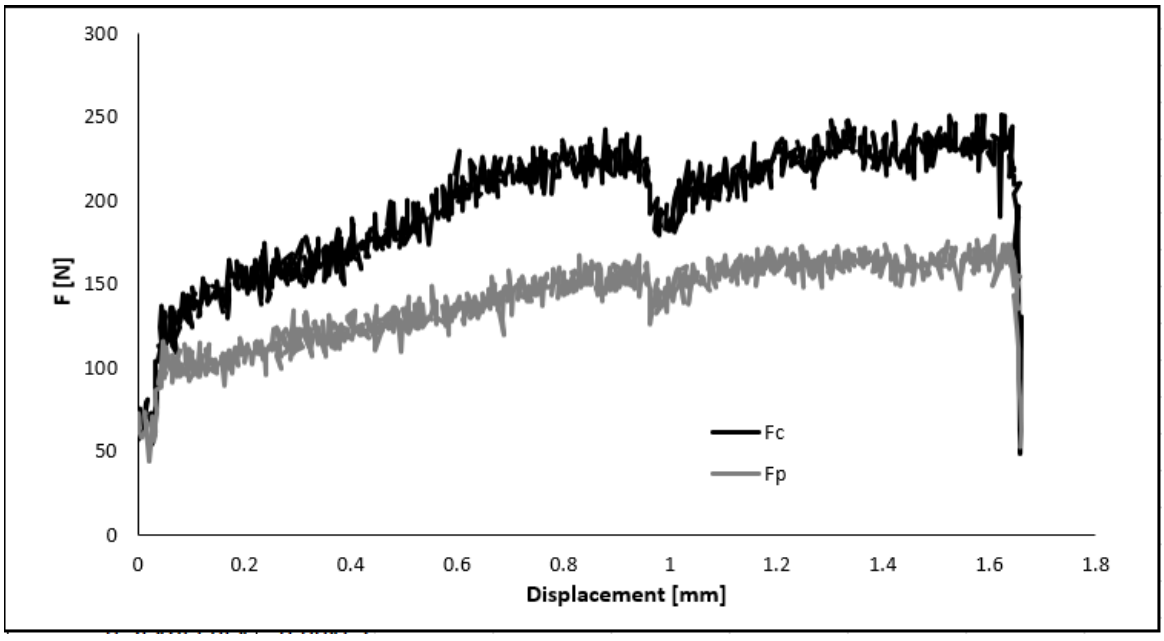

Figure 3-6 - Cutting test forces of the AA1050 cutting test performed

In order to successfully perform orthogonal cutting tests, the following statements have to be met (section 2.3):

1. Constant cutting speed, which was verified during the cutting test;
2. Cutting in stationary conditions, which can be seen in figure 3-6 – constant cutting forces;
3. Plane strain conditions - i.e. the specimen must be wide enough to prevent lateral deformation: $\frac{b}{e} \geq 5$, which is verified (on the used specimen, $\frac{b}{e} = 250$);

4. The workpiece material is isotropic and homogeneous – verified by AA1050;
5. Cutting speed is perpendicular to the cutting edge– verified by the cutting tool fixation developed by Andrade (2019).

In conclusion, the developed orthogonal cutting machine is capable of performing low speed orthogonal cutting tests. In addition, the cutting and penetration forces' peak values are equal to those obtained by Andrade (2019) under the same test conditions (approximately 200N and 150N, respectively).

3.2. Ring Compression Tests Equipment

The ring compression tests were performed on a customized split Hopkinson pressure bar (SHPB) – similarly to (Hartley, *et al.*, 2006) - which can provide a wide range of strain-rate conditions. The main components can be divided into three groups, as shown on figure 3-8 impact bench, a pneumatic gun (to provide the necessary power for the high-speed tests) and a hydraulic ram cylinder (to perform the low-speed tests). The impact bench is composed of basic structural parts and two compression platens made of WC-Co, with a nano composed PVD coating, HiPIMS of TiAlSiN technology and 3 thickness micrometers (provided by Palbit, SA). The compression platens used in the experimental tests have been machined and polished to limit surface roughness below $Ra < 0.1\,\mu m$. To generate the aimed temperature (up to 400ºC), a furnace was placed around the compression platens.

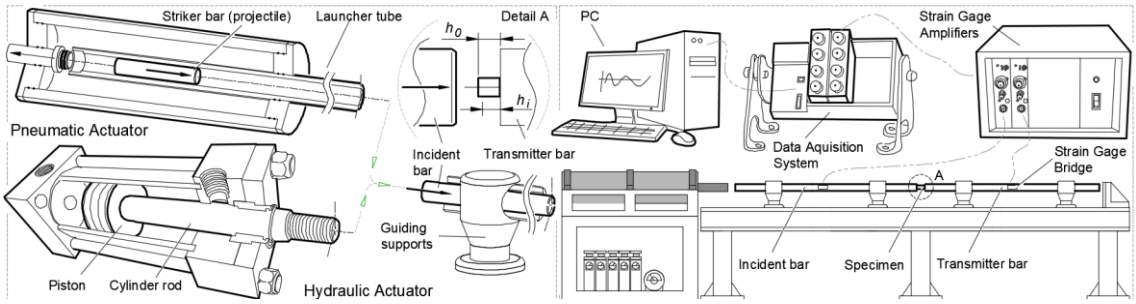

Figure 3-7. Schematic representation and nomenclature of the specially designed split-Hopkinson pressure bar that allows simultaneously quasi-static and high strain rate testing conditions by using (a) replaceable pneumatic and hydraulic actuators; (b) assembled on the same platform as the downstream data acquisition elements – which were not used on the ring compression tests

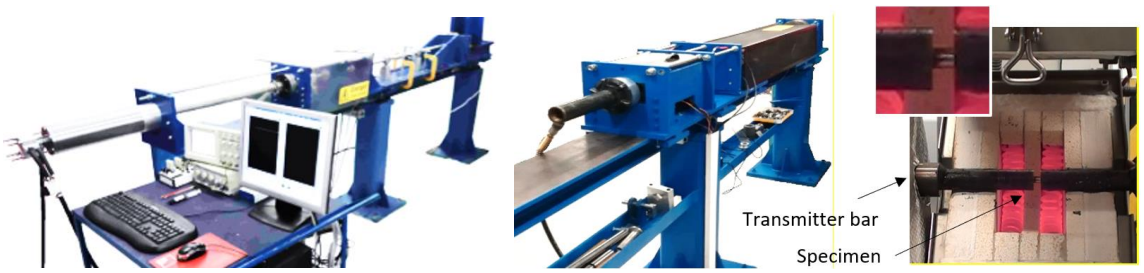

Figure 3-8. Split-Hopkinson pressure bar that was utilized in the ring compression tests; (a) Configuration using the pneumatic actuator; (b) Using the hydraulic actuator; (c) Compression platens

The inner diameter, outer diameter and height of the ring-shaped specimens were measured before, during and after the experiments using a digital Vernier caliper. A microscope was also used to confirm these values, using diascopic illumination and Solidworks 2018 software to perform the measurements on the images of the specimens.

3.3. Material and Plan of Experiments

The material used for both the orthogonal cutting and ring compression experiments is the 18Ni300 maraging steel, obtained through two different processes: conventional and additive manufacturing (horizontal direction, by laser powder bed fusion, LPBF). It has an elastic modulus of 190 GPa and a Poisson modulus of 0.3. Its plastic properties will be better described on the next chapter, as uniaxial compression experiments were carried out at different temperatures and strain rates in order to characterize its plastic behavior under realistic operative conditions.

Besides, orthogonal cutting and ring compression experiments were also carried out. The orthogonal cutting experiments were performed on both AM and conventional maraging specimens at low cutting speeds (between 0.08 and 26.1 $m.min^{-1}$) and dry conditions. Some tests were performed with collaboration with FEUP, and some in IST. The detailed plan of experiments is shown below:

Location	***e* [mm]**	**V [$m.min^{-1}$]**	**Material**
FEUP	0.3	26.1	AM + C
FEUP	0.15	26.1	AM + C
IST	0.15	0.08	C
IST	0.1	0.08	C
IST	0.05	0.08	C

Table 3-1. Orthogonal cutting plan of experiments (AM - additivelly manufactured; C - conventional).

The ring compression experiments were performed on the same material: 18Ni300 steel, both conventional and additively manufactured, but under different temperatures and strain rates. However, before performing dry ring compression tests, lubricated ring compression tests were carried out to correct the σ-ε curves (detailed on the next chapter). Three different lubricated ring compression tests were carried out in the three most “extreme” combined strain rate-temperature conditions: quasi-static (QS) at room temperature (RT – approximately 25ºC), QS at 400ºC, 6000 s^{-1} at 400ºC.

Once obtained the final corrected σ-ε curves, the dry experiments on maraging steel specimens (both conventional and additively manufactured) were carried out at RT, 200ºC and 400ºC, and using three different strain rates: QS, 300 s^{-1} (V1) and 6000 s^{-1} (V2).

The ring compression experiments are detailed in tables 3-2 and 3-3 below. Due to the high cost per Kg of AM maraging steel, only two different strain rates were tested (the lowest one, QS, and the highest one, 6000 s^{-1}).

v/T	25ºC	200ºC	400ºC
Q.S.	Dry + Lub	Dry	Dry + Lub
V1	Dry	Dry	Dry
V2	Dry	Dry	Dry + Lub

Table 3-2. Plan of experiments for the conventional maraging specimens

v/T	25ºC	200ºC	400ºC
Q.S.	Dry + Lub	Dry	Dry + Lub
V2	Dry	Dry	Dry + Lub

Table 3-3. Plan of experiments for the AM maraging specimens

4. Theoretical Development

This chapter presents the finite element models (FEM) developed for the present work in order to obtain the ring compression calibration curves, as well as the experimental-numerical methodology adopted. An orthogonal cutting model will also be presented.

4.1. Stress-Strain Curves Correction

In order to build the calibrated curves, it is necessary to find the materials flow stress, for each temperature and strain-rate tested condition. This task was performed through the compression of cylindrical specimens (Φ 4 x 4mm). Despite using graphite as lubricant in order to minimize friction, the obtained strain-stress curve is not frictionless. Figure 4-1 illustrates the procedure adopted for obtaining the frictionless flow stress. Firstly, compression tests for all combinations of strain-rate and temperature were performed under lubricated conditions, enabling the identification of a preliminary flow stress represented as “original” in figure 4-1 (first image). Secondly, ring compression tests were performed exactly for the same conditions of the cylindrical compression tests and preliminary calibration curves were numerically obtained using the preliminary flow stress, allowing for the identification of the friction coefficient (c.f.1) of the ring test, as shown in figure 4-1 (second image). Finally, the cylindrical compression test was numerically simulated inputting the obtained friction coefficient and enabling the correction of the strain-stress, through subtraction of the friction overestimation of the c.f.1 curve. The corrected (frictionless) stress-strain curve is thus obtained, as illustrated in figure 4-1 (third image).

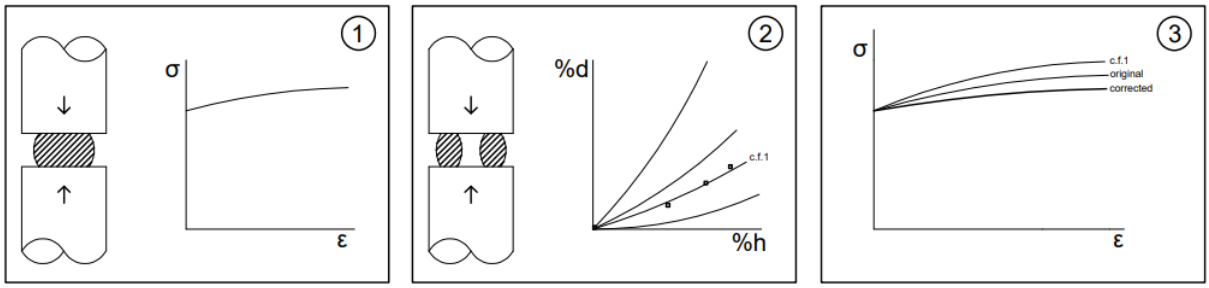

Figure 4-1. Flowchart explaining the process used to obtain the stress-strain curves corresponding to frictionless conditions

The compression model (used on step 3), and the ring compression model (used on step 2, and to generate the final calibration curves) will be described in the upcoming sections.

4.2. Compression Model

To perform step 3 of figure 4-1, a uniaxial compression model was developed using a commercial FEA software with the implicit method. An axisymmetric model was created, with a Φ 4 x 4 mm 2D deformable workpiece (the same dimensions of the specimen used to obtain the experimental σ-ε curve). However, to reduce the computation time, only a quarter of the operation was considered (i.e., a Φ 2 x 2 mm workpiece was created). An analytical rigid part (to serve as the punch) was also created, as well as a mesh with 2500 axisymmetric elements with reduced integration, as shown in figure 4-1.

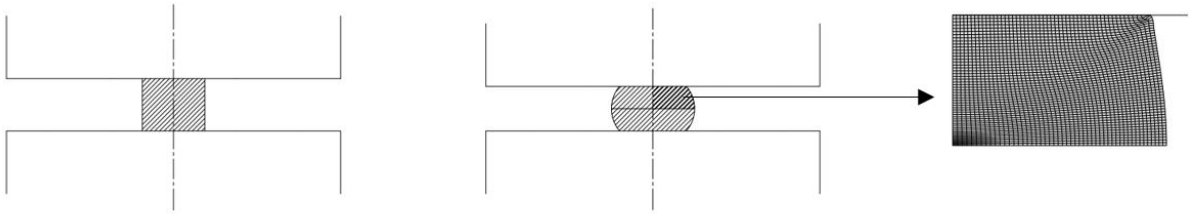

(a) (b) (c)

Figure 4-2. Finite elements model of the uniaxial compression test: (a) Scheme of the non-deformed specimen; (b) Scheme of the deformed specimen, highlighting the modelled zone of the axisymmetric process; (c) Deformed mesh of the developed finite elements model

To validate the proposed compression model, three materials were tested. First, a rigid-perfectly plastic material was tested (σ_y = 1 MPa, E = 1 GPa, σ_u = 1 MPa), and secondly, an elastic-plastic material (σ_y = 1 MPa, E = 10 MPa, σ_u = 1.3 MPa) was tested. In both simulations, the friction coefficient considered was zero (frictionless conditions), and a Poisson's ration of 0.3 was used. The default Amonton-Coulomb's friction model was used (on both simulations – uniaxial cylinder compression and ring compression), due to its simplicity and adequacy and computational time savings. The results are shown in figure 4-3.

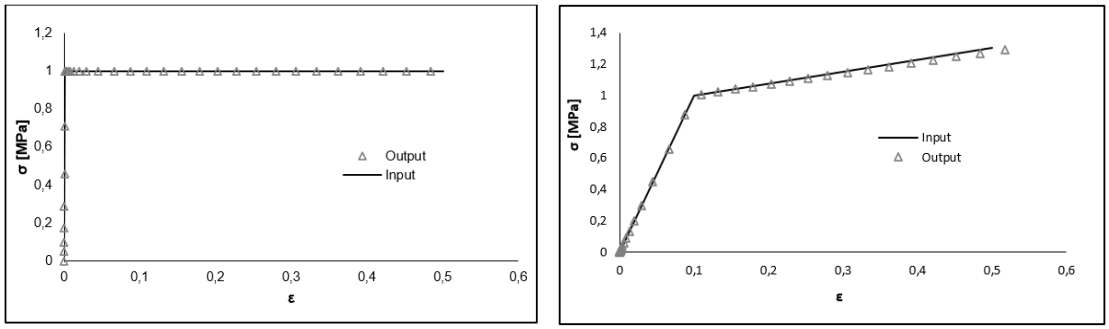

(a) (b)

Figure 4-3. Comparison between input behavior and the corresponding output strain-stress curve for the cases of a (a) elastic-perfectly plastic material; (b) elastic-plastic material.

As shown in the graphs above, the proposed model seems to be appropriate for simulating simple materials' behavior. A real material (AA1050) was also tested using this model. The obtained σ-ε curve is shown in figure 4-4.

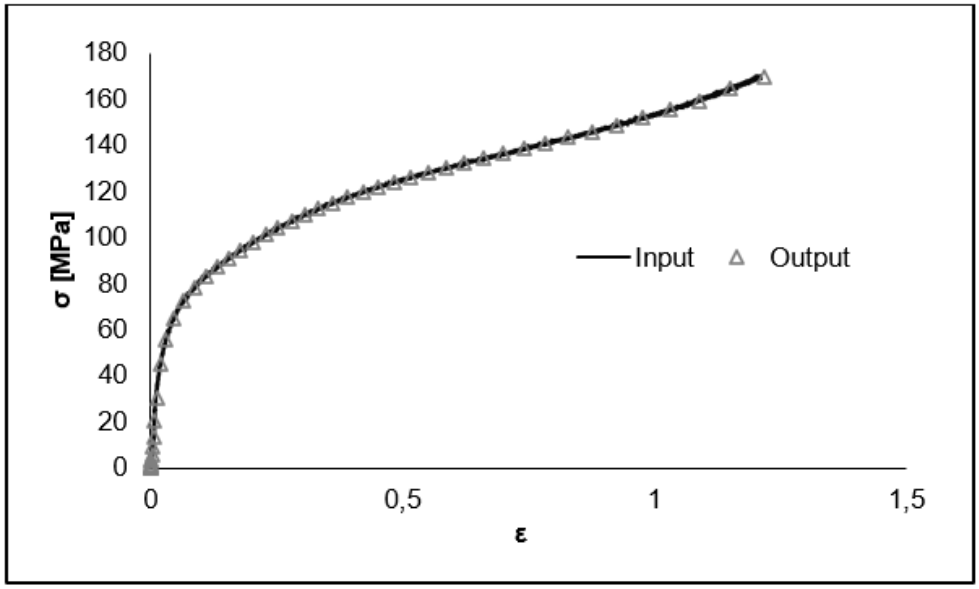

Figure 4-4. Comparison between the input behavior of AA1050 and the obtained output strain-stress curve

The simulation's resulting σ-ε curve confirms that the proposed model is appropriate to simulate compression of elastic-plastic materials with work hardening.

4.3. Ring Compression Model

The ring compression model is very similar to the one used in the previous section (axisymmetric, only considering one quarter of the operation, with a 2D deformable workpiece and a rigid tool). However, there is a space between the symmetry axis and the workpiece, to form the cross section of the ring. A mesh with 3750 axisymmetric elements was generated, as shown in figure 4-5.

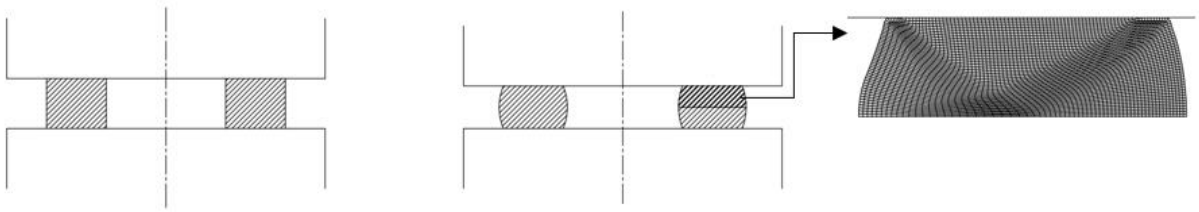

Figure 4-5. Finite elements model of the ring compression test: (a) Scheme of the non-deformed specimen; (b) Scheme of the deformed specimen, highlighting the modelled zone of the axisymmetric process; (c) Deformed mesh of the developed finite elements model

To validate the proposed ring compression model, the same material used by Cristino *et al.* (2010) was used (pure lead - 99.9%). The workpiece is a ring respecting the 6:3:2 ratio (outside diameter – 24 mm, inside diameter – 12 mm, height – 8 mm), and the rigid tool has a constant speed of 1.7 $mm.s^{-1}$, which is the equivalent to a strain rate of 0.2125 $s^{-}1$. The yield stress of this material is given by:

$$\bar{\sigma} = 19.2\dot{\varepsilon}^{0.042} - 12.0\dot{\varepsilon}^{0.052}\exp^{(0.68\dot{\varepsilon}-7.34)\varepsilon} \quad (25)$$

Using this value for the strain rate, and MATLAB 2015 to solve the equation (16) for 5000 points, the mechanical behavior was inserted in the software. Five simulations were performed at five different friction factors. The results are displayed in figure 4-6.

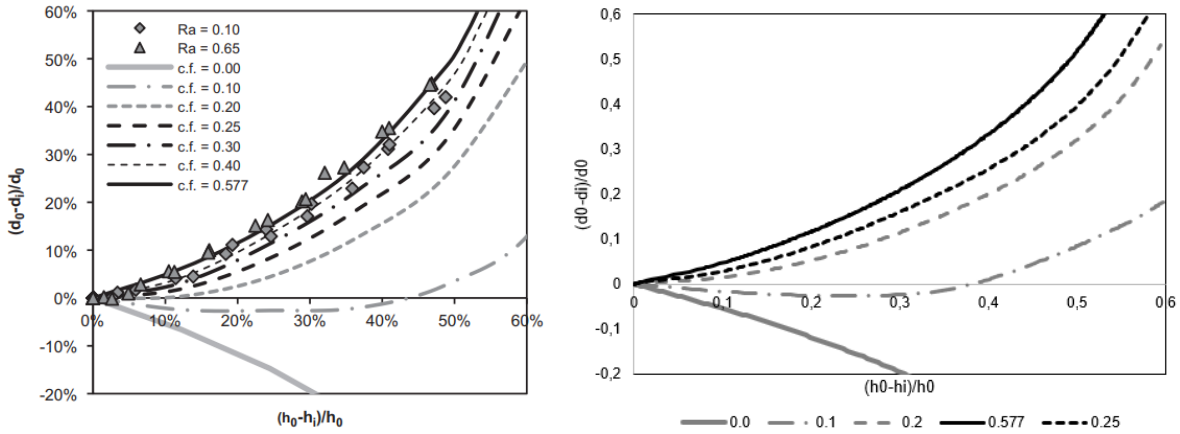

(a) (b)

Figure 4-6. (a) Calibration curves for pure lead (99.9%) used by Cristino (2010); (b) Curves obtained using the proposed model

As shown in figure 4-6, comparing to the calibration curves obtained numerically by Cristino (2010), the developed finite elements model for the present research follows the frictional behavior of pure lead (99.9%) and can be used for the ring compression simulations carried out on chapter 4.

4.4. Orthogonal Cutting Model

For the present work, an orthogonal cutting model was developed as well, to complement and better understand the experiments performed. The mesh is composed of 2548 elements without reduced integration, and was elaborated on the same FEA software as the previous models, in order to better simulate quasi-static plastic deformation phenomena. The cutting tool was considered as a rigid body, and has a rake angle of $\alpha = 5^{\circ}$. The only model that converged successfully is presented in figure 4-7, and is composed of three distinct zones: one with a defined damage criterion (2), and two zones without a defined damage criterion (1). This allows the existence of a sacrificial layer (2), that will be only damaged zone of the model in the process of cutting, in order to separate the chip from the uncut part of the specimen. For the damage criterion, a ductile damage was adopted, with a fracture strain of 0.1, and a displacement at failure value of 0.012 mm (obtained by multiplying the fracture strain by the length of an element).

Contrarily to what is common among investigators that use the explicit method to develop orthogonal cutting models, no adaptive mesh was used for the present model, as mesh convergence was severely compromised when it was present.

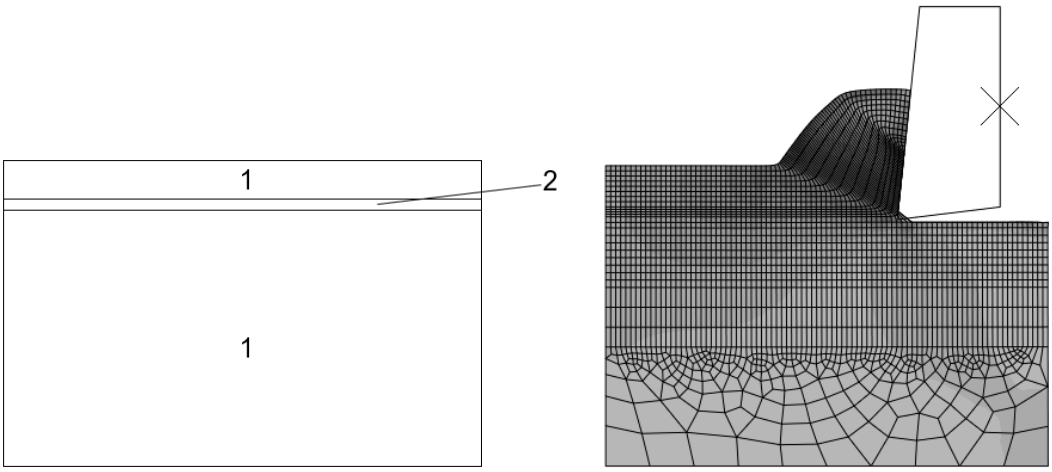

Figure 4-7. Orthogonal cutting model developed: (a) Three distinct mesh zones, one with a damage criterion (2), and two without a defined damage criterion (1); (b) Deformed mesh.

5. Results and Discussion

This chapter presents the results of the present work are shown. In the first section, the orthogonal cutting tests results performed on maraging are shown. In the second section, the ring compression tests and its resulting friction coefficient's values are shown and discussed in detail, being the most relevant results obtained throughout the present dissertation. Finally, a comparison between the values obtained on both experiments will be presented.

5.1. Orthogonal Cutting Results

The orthogonal cutting results presented below were obtained with close collaboration with FEUP, at cutting speeds of 26.1 $m.min^{-1}$, and using a tungsten carbide tool with $\alpha = 5º$ and $\sigma = 7º$, and with the same coating of the compression platens. As shown in figure 5-1, it was possible to measure orthogonal cutting forces and quasi-stationary conditions were obtained, with just a slight increase of the forces along the process.

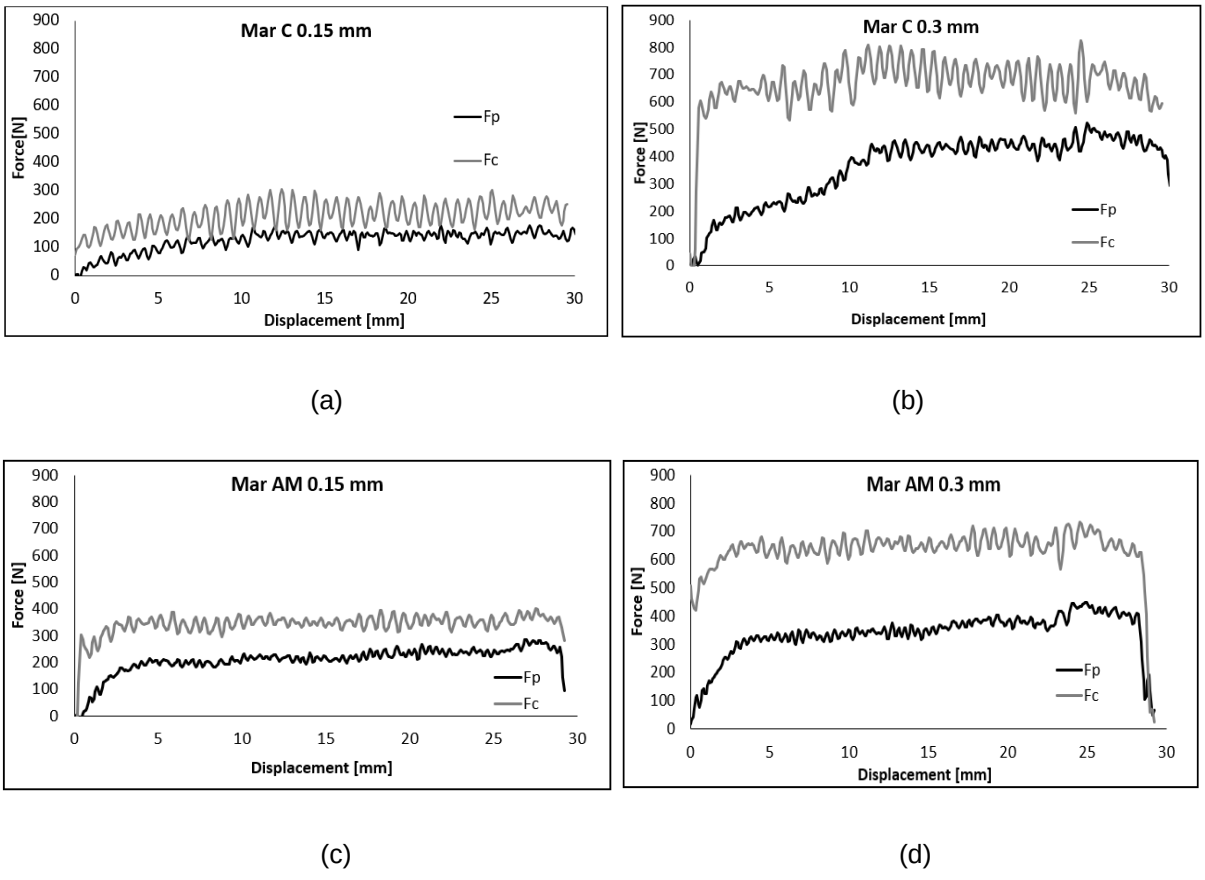

Figure 5-1. Cutting forces vs displacement on (a) Conventional maraging at e = 0.15 mm; (b) Conventional maraging at e = 0.3 mm; (c) AM maraging at e = 0.15 mm; (d) AM maraging at e = 0.3 mm

As present in figure 5-1, cutting forces increase with an increase of the depth of cut. However, for both depths of cut (0.1 mm and 0.3 mm), the values of the cutting forces are higher for conventional maraging specimens. Despite being easier to machine and producing lower cutting forces and tool wear, AM

maraging has a higher yield friction than the conventional material, and this phenomenon persists under higher temperatures and strain rates. This topic will be covered on the next section of the present work.

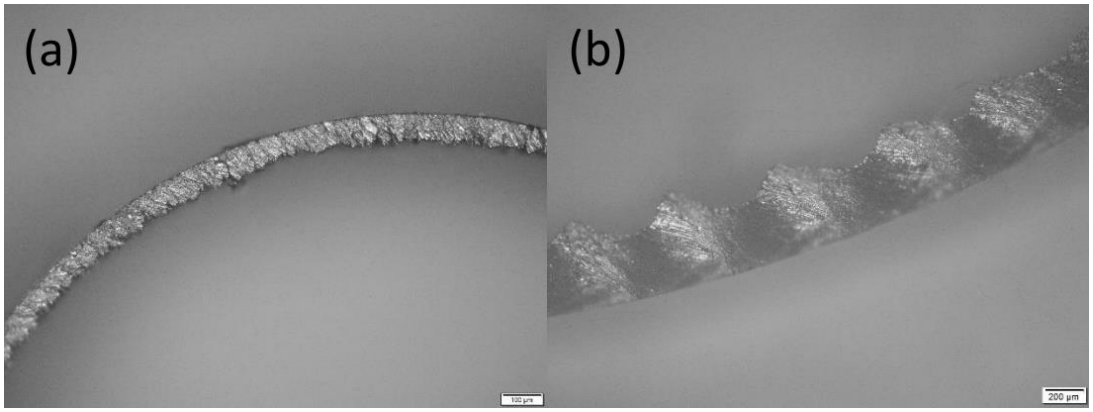

Figure 5-2. Chips from of AM maraging for extremely different depths of cut; (a) e = 0.03 mm; (b) e = 0.3 mm

As shown in figure 5-2, segmented chips start to occur for higher depths of cut, for both conventional and AM maraging specimens. Regarding the tribology of the process, the friction coefficient values were obtained by (20), and are presented on table 5-1 below.

Condition / e	**0.15 mm**	**0.3 mm**
Conventional	0.713	0.666
AM	0.704	0.642

Table 5-1. Friction coefficient values obtained on the orthogonal cutting tests performed in collaboration with FEUP

As shown on table 5-1, the friction coefficient decreases with an increase of the depth of cut, for both materials. However, no conclusions can be directly inferred regarding the influence of the metallurgical condition (AM vs conventional processing) on the friction coefficient. Moreover, all the friction coefficient values are above the theoretical limit of $\mu = 0.577$, which raises some questions about the values obtained on the orthogonal cutting experiments, as well as the physical mechanisms and explanation behind them. Consequently, it was not regarding its tribological characterization and comparison on orthogonal cutting tests, which led to an investigation about its tribological behavior under more extreme operative conditions, as detailed on the next section.

To complement these orthogonal cutting tests, additional tests were performed on AM maraging specimens at IST with the same cutting tool, but with α = 0º. Three depths of cut were tested, 0.05 mm, 0.1 mm and 0.15 mm depths of cut, and at very low cutting speeds (0.08 $m.min^{-1}$). The obtained friction coefficients are shown in table 5-2.

Depth of Cut	**0.05 mm**	**0.1 mm**	**0.15 mm**
Friction Coefficient	0.590	0.596	0.606

Table 5-2. Friction coefficient values obtained on the additional orthogonal cutting tests performed on IST

As represented on table 5-2, the friction coefficients obtained at very low speeds are lower than the ones obtained at higher speeds by over 0.1, which suggests that the friction coefficient increases with the strain rate on the AM maraging steel.

In order to better understand the high friction coefficient values present on all the orthogonal cutting tests performed, a complementary simulation was performed using the quasi-static conventional maraging's flow curve at room temperature as the material input. However, the mesh did not converge for friction values superior to 0.32, as expected on a model developed on the FEA software. Despite this fact, the results shown on figure 5-3, obtained with μ = 0.32, e = 0.15 mm, present the same cutting force values obtained on the orthogonal cutting test performed at the same depth of cut (figure 5-1). The penetrative force is significantly lower, but this fact is due to the well-known problems of numerical simulation software to obtain realistic values for F_p. This aspect raises even more questions regarding the friction coefficient's values obtained on the cutting experiments, and thus led to the ring compression experiments at different conditions presented on next section, to explore the influence of temperature and strain rate on the friction coefficient.

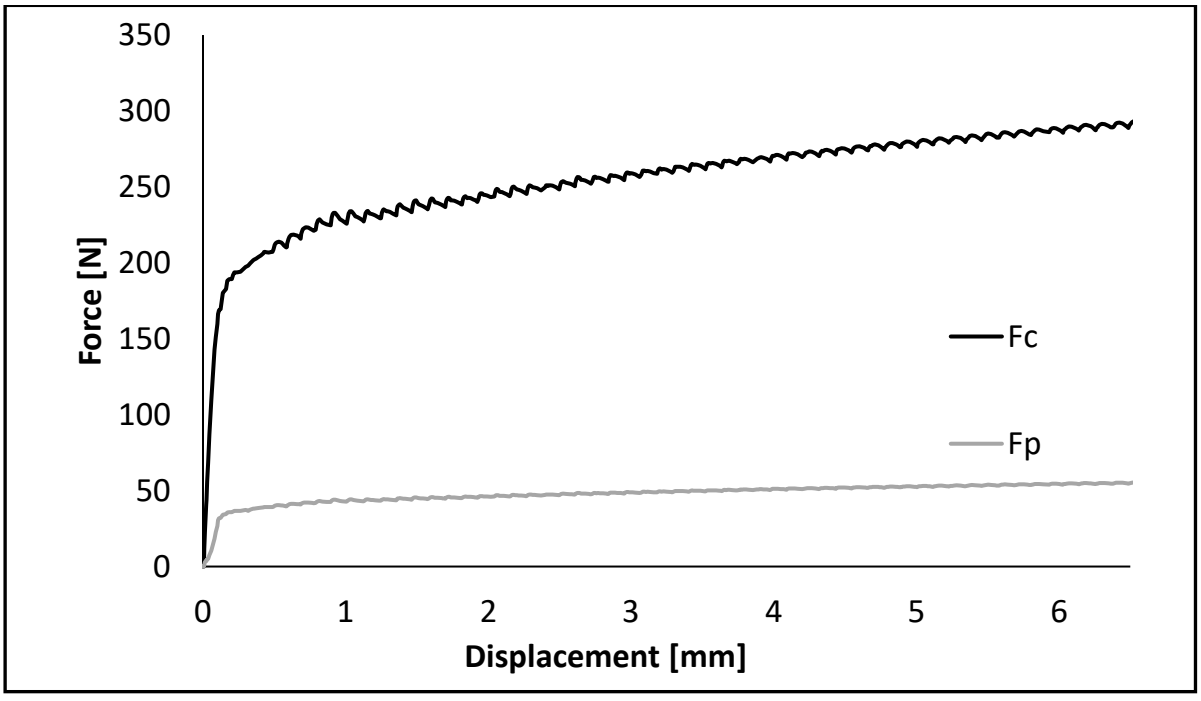

Figure 5-3. Cutting and penetrative forces obtained on the numerical simulation performed

5.2. Ring Compression Results and Friction Assessment

This section intends to explore the influence of temperature and strain rate on the friction coefficient. The corrected flow curves are shown. Then, the final calibration curves are represented simultaneously with the dry ring compression measurements. Finally, in the last subsection, the friction coefficients obtained are shown, as well as their variation with temperature, test speed and metallurgical condition.

5.2.1. Corrected σ-ε Curves

To obtain the calibration curves, the σ-ε curves obtained by applying the procedure described in section 4.1 corresponding to frictionless conditions are inserted in the FEA software as an input. Two of these curves are shown below in figure 5-4. The other corrected are present in the attachments.

As shown in figure 5-4, the original σ-ε curves have, not only different aspects, but also different strain hardening exponents (the more temperature and strain rate, the more positive the strain hardening exponent). Besides, as expected, the bigger the friction coefficient used to correct the σ-ε curve, the bigger the distance between the original and the corrected curve.

Regarding the AM and conventional processing conditions, the yield stress values present on the AM experiments are slightly higher than the ones obtained on conventional specimens, which suggests that maraging steel specimens increase their mechanical strength when obtained through additive manufacturing

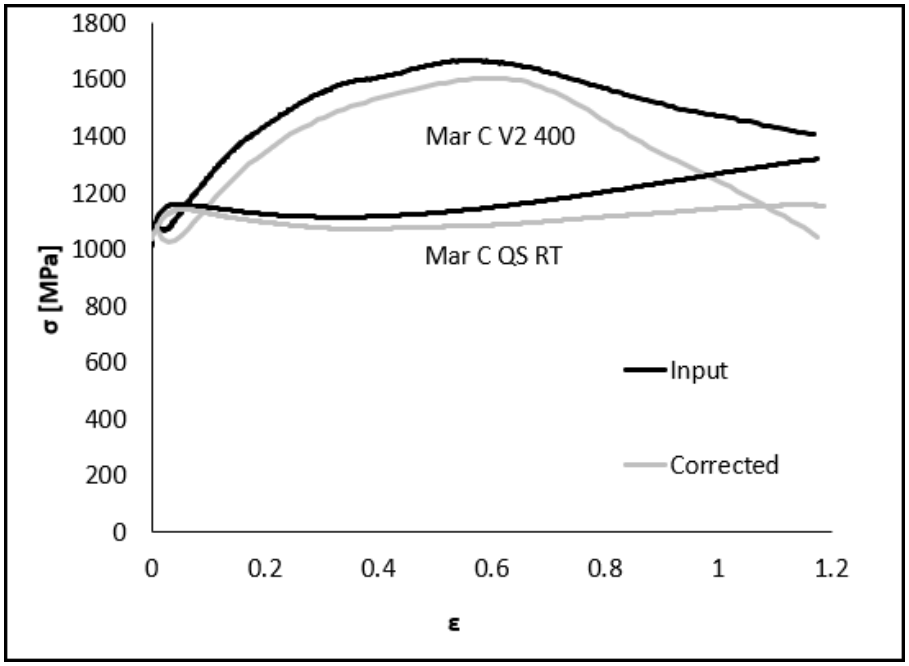

Figure 5-4. Original and corrected stress-strain curves for conventional maraging at 6000 s-1 (V2) and 400ºC conditions, corrected with μ = 0.13, and at quasi-static (QS) and 25ºC (RT) conditions, corrected with μ = 0.09

5.2.2. Ring Compression Tests

The ring tests were successfully performed on the equipment described in section 3.2 (SHPB). The highest deformation (>50%) occurred for higher test speeds, being 20% - 30% height reduction the most common values for quasi-static tests. On combined higher speed and temperature experiments, some of the specimens were impossible to measure due to the occurrence of crack formation (figure 5-5). This phenomenon occurred more frequently on higher strain rate conditions.

(a) (b) (c) (d)

Figure 5-5. (a) Ring specimen before the experiment; (b) Ring specimen after the experiment; (c) Ring specimen before the compression test on an axial view; (d) Fractured ring specimen after a high temperature and high speed experiment

Another noticed phenomenon is the fact that the maraging specimens significantly increase their mechanical strength on temperatures above 400ºC (the ring suffered a maximum 10% height reduction on such conditions), as expected, according to some investigators (Lohmann, *et al.*, 2019). That was the main reason that led the ring compression experiments to be performed under 400ºC. Another relevant note is the good performance of the WC-Co compression platens, which are recommended to perform ring compression tests at higher strain rates and temperatures, and allowed a tribological study on a metal-ceramic interface without losing its low roughness and high rigidity. To quantify the friction coefficient values between the compression platens – maraging steel interface, the calibration curves obtained numerically (using the σ-ε curves presented on the last section as the input) were compared to the experimental results. Two of these calibration curves, QS 200ºC and V2 200ºC, are shown in figure 5-6 below. The full results are shown in the attachments of the present work.

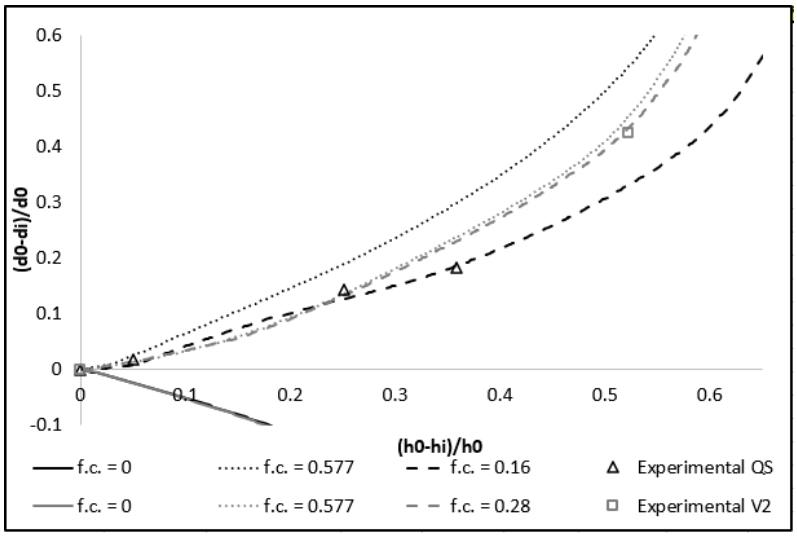

Figure 5-6. Calibration curves and experimental results of ring compression tests for conventional maraging specimens at 200ºC and two different strain rates: QS and 6000 s-1 (V2)

In relation to the calibration curves, two phenomena were observed: the calibration curves are affected by the inserted σ-ε curve (as shown in figure 5-6, the curves corresponding to a friction coefficient of 0.577 are different), and in the high-speed σ-ε curves, the difference between the calibration curves

corresponding to a higher friction coefficient (> 0.2) is smaller than in the quasi-static ones, as represented in the calibration curves of V2 200 maraging in figure 5-6. This last aspect made higher friction coefficient values harder to obtain accurately on high-speed experiments, which is also reported by Cangundo (2009). However, besides the difficulty of reading accurate results for higher friction coefficients, it was possible to understand a clear tendency of the friction coefficient's variation with temperature and speed, as discussed on the next subsection.

5.2.3. Friction Coefficient's Variation

The chosen low roughness of the compression plates intends to promote the adhesion contribution to the friction coefficient, μ_a, and reducing other contributions (plowing, etc…). This fact allows a more precise study and conclusions about the friction coefficient's variation on the chosen interface, as μ_a is the main effect present on the total friction coefficient, μ, as shown in (2).

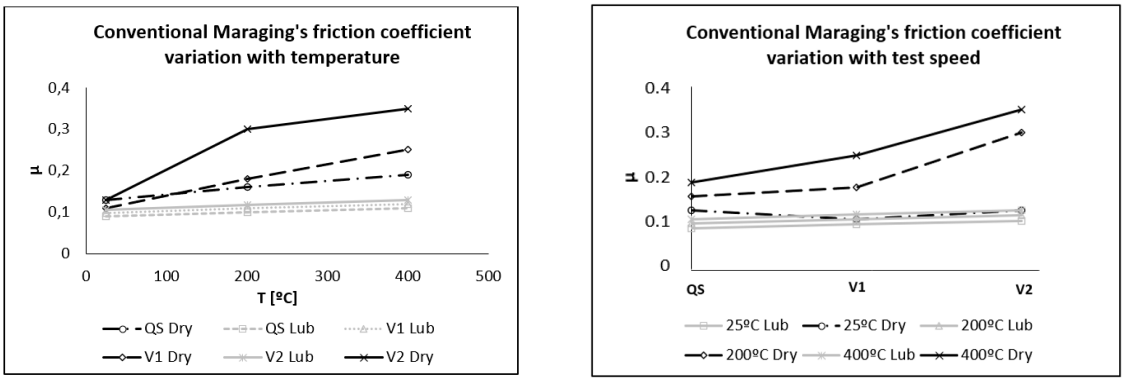

(a) (b)

Figure 5-7. Friction coefficient results for conventional maraging specimens shown in a graph of μ vs (a) Temperature; (b) Test speed

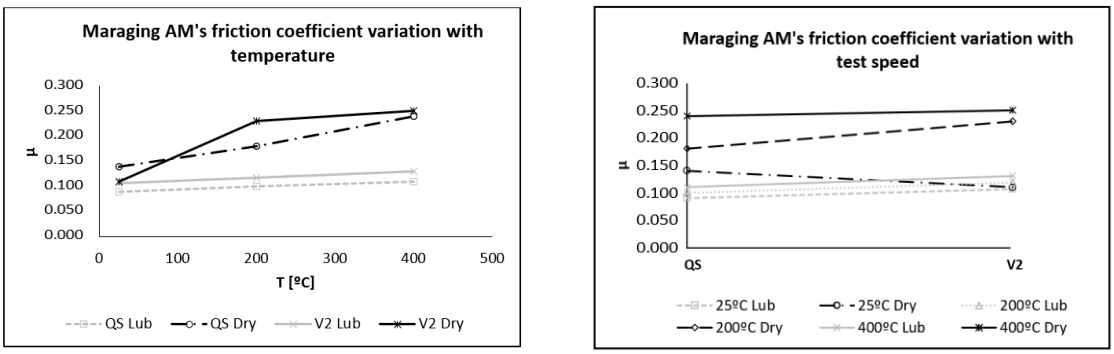

(a) (b)

Figure 5-8. Friction coefficient results for AM maraging specimens shown in a graph of μ vs (a) Temperature; (b) Test speed

The resulting friction coefficient values as a function of temperature, strain rate and metallurgical condition are presented in figure 5-8 above (both the dry tests, and lubricated experiments used to correct the σ-ε curves). Excluding a few exceptions (the 25ºC tests for both AM and conventional maraging), the friction coefficient is higher in the dry tests than in the lubricated tests, which indicates

that the use of graphite as lubricant on a maraging – WC-Co interface reduces friction significantly, even at higher temperatures and strain rates, suggesting that two lubricated surfaces with low roughness have a decrease on adhesion phenomena. This same result is proposed by Bhushan (2003). However, the friction on lubricated tests becomes slightly higher, the higher the temperature and test speed, which suggests lubricant degradation starts to occur.

On the dry experiments, the higher the test temperature, the higher the friction coefficient in both metallurgical conditions (conventional and additively manufactured material), with variations sometimes surpassing 50%. This same result is suggested by Bhushan (2003), when adhesion is the main friction mechanism present on a solid-solid interface, due to an increase of ductility and area of contact with an increase in temperature. However, in both AM and conventional specimens, there is a lower difference between the friction coefficients at 200ºC and 400ºC, for a strain rate of 6000 s^{-1} (V2) – variations inferior to 20%.

The friction coefficient also tends to vary with test speed: for conventional maraging, it clearly increases with test speed for higher temperatures (200ºC and 400ºC), which is the opposite result obtained by Sun (2020) when performing pin-on-disc tests on maraging specimens. In addition, the strain rate is found to be a more influential factor on the friction coefficient than temperature on the present dissertation, which also goes against the results found by Börder (2005) on steel specimens. However, for AM maraging, the friction coefficient's variation with speed becomes inconclusive, as it decreases with speed at room temperature tests, increases at 200ºC, and is approximately constant at 400ºC. Combined higher temperatures and test speeds also seem to produce higher friction coefficients (variations superior to 50% at V2), in both materials. In the other hand, the metallurgical condition doesn't seem to affect neither the tendencies of the friction coefficient's variation, nor its values, as much as temperature and test speed do. However, by analyzing some of the experimental measurements, the friction coefficient varies along the compression test, as shown in figure 5-9.

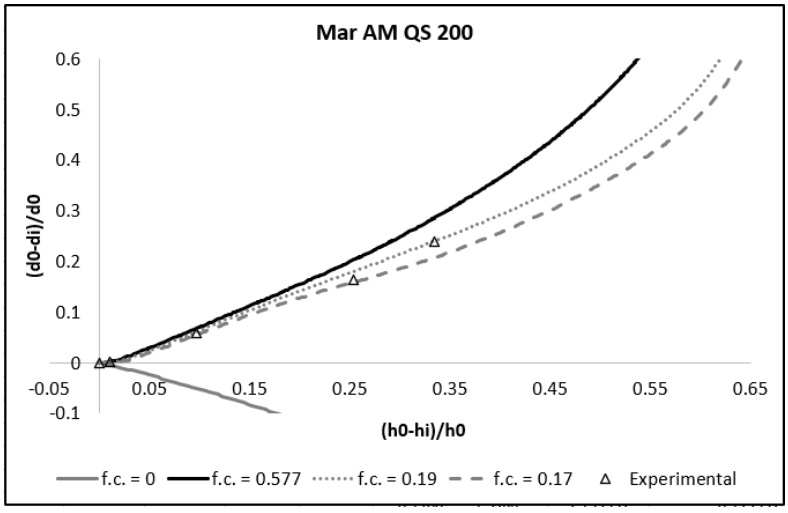

Figure 5-9. Variation of the friction coefficient along the ring compression test

A quasi-static experiment was used to support this fact, as more accurate measurements are possible to obtain during this type of test. This reduction of the friction coefficient is most certainly due to the oxides present on the specimen's surface, that become less relevant as the ring expands, thus increasing the friction coefficient along the process (the adhesion between a metal-ceramic interface is higher to the adhesion between an oxide-ceramic interface). This phenomenon has already caught the attention of some investigators, such as Cristino (2007). The author used an argon-rich atmosphere successfully in order to reduce its initial percentage on the test interface, thus allowing to obtain friction coefficient values exclusively of a solid-solid interface.

To complement figure 5-9, that demonstrates the friction coefficient increase during the process due to the percentage of oxide present on the specimen's surface along the process, the friction coefficients of the oxide-ceramic and metal-ceramic interfaces will be estimated. In order to proceed with the calculations, the percentage of oxide and pure metal present in the surface need to be obtained. For that purpose, assuming that initially the surface is 100% oxide, and the percentage of oxide present will decrease with the area expansion during the process, the following formulas are proposed:

$$O = \frac{A_i}{A_f} \tag{26}$$

$$P = 1 - O \tag{27}$$

Where A_f is the area of the ring specimen's surface at the end of the experiment, A_i is the area of the specimen before the compression test, O is the fraction of oxide present on the surface at the end of the compression, and P is the fraction of pure metal at the end of the process. The estimation of the friction coefficient is then obtained by:

$$\mu = P.\mu_M + O.\mu_O \tag{28}$$

where μ_M and μ_O are the friction coefficient of the metal-ceramic and oxide-ceramic interfaces, respectively. Using the experiment represented in figure 5-9, the following values can be obtained:

$$\begin{cases} O_{initial} = 1.0 \\ P_{initial} = 0.0 \\ O_{end} = 0.340 \\ P_{end} = 0.659 \end{cases}$$

Thus, knowing from figure 5-9 that $\mu_{initial} = 0.17$ and $\mu_{end} = 0.19$ using (28) at the beginning and at the end of the process with these values, we obtain:

$$\begin{cases} \mu_O = 0.17 \\ \mu_M = 0.229 \end{cases}$$

Therefore, demonstrating a significant difference between the friction coefficients present on metal-ceramic and oxide-ceramic surfaces, which suggests a variation of the friction coefficient during a ring compression experiment.

5.3. Orthogonal Cutting and Ring Compression Comparation

The friction coefficient values obtained on the ring compression experiments demonstrated a clear variation with temperature and strain rate. The conventional maraging specimens presented an increase on the friction coefficient with temperature and test speed, and the additively manufactured ones demonstrated the same tendency with temperature, despite not allowing to take direct conclusions regarding the strain rate influence. The metallurgical condition also didn't seem to influence the friction coefficient values.

On the orthogonal cutting tests, much higher friction coefficient values were obtained, comparatively to the ring compression experiments (0.1 – 0.3 vs 0.6 – 0.7). However, as different strain rates were tested on the AM specimens, its influence on the friction coefficient on the orthogonal cutting experiments can be obtained. Figure 5-10 demonstrates this variation - the strain rates were calculated using (23), where Δy was obtained using the cutting numerical model developed, as suggested by Thimm *et al.* (2020).

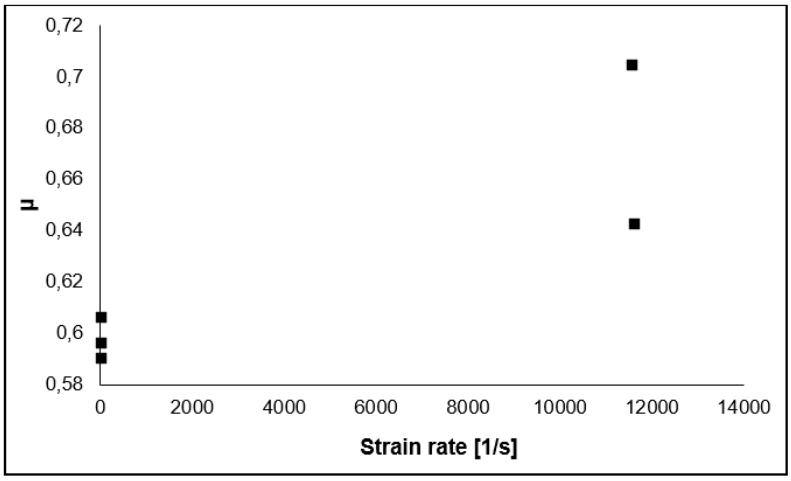

Figure 5-10. Variation of the friction coefficient with strain rate on the orthogonal cutting tests performed on AM maraging specimens

As shown in figure 5-10, the friction coefficient clearly increased with the strain rate on orthogonal cutting experiments, therefore dissipating the inconclusive results obtained on ring compression tests performed on AM specimens. The combined ring compression – orthogonal cutting tribology study demonstrated that the temperature and strain rate are influential factors on the friction coefficient present on the studied interface. However, the ring compression experiments have proven to be a much simpler way to evaluate the tribological condition on a given interface, and inclusively allowed the study of the strain rate and temperature as independent factors influencing the process, which was not possible to do on orthogonal cutting tests. The same simplicity difference was present on the simulations performed, as computational time and mesh convergence were significantly easier to obtain on the uniaxial compression numerical models and simulations.

6. Conclusions and Future Developments

This final chapter presents the conclusions of this investigation, as well as the future works suggested to students and authors that intend to investigate the discussed themes.

6.1. Conclusions

The present work intended to study the tribological behavior of a new engineering material: the 18Ni300 maraging steel. For the effect, orthogonal cutting and ring compression experiments were performed on it.

Answering the questions presented on the introduction, the combined approach between ring compression tests and the FEA software disclosed that the friction coefficient tends to be higher, the higher the temperature and the test speed. The metallurgical condition (conventional vs AM maraging) didn't seem to affect its value as much. The zero roughness of the compression platens intended to isolate the phenomena of adhesion, in order to minimize the effect of other contributions. Still, some variations of the friction coefficient along the process were found, and the presence of oxides on the surface of the material tends to be the main cause, as no controlled atmosphere was used. The same friction coefficient variations with strain rate and metallurgical condition found on ring compression experiments were observed on AM specimens the orthogonal cutting tests.

Another conclusion that can be taken is the fact that there are no significant performance differences between AM and conventional maraging. The higher cost per Kg of AM maraging reflects on more complex attainable geometries and better machinability, without losing mechanical strength and tribological performance under extreme conditions.

As a final note, this overall investigation also intends to raise awareness to the fact that the tribological conditions may be affected by service conditions (i.e., temperature and strain rate), particularly in new engineering materials with few studies and general mechanical knowledge and characterization, such as the maraging steel.

6.2. Future Works

Relatively to the orthogonal cutting machine, although many problems that were reported by Andrade (2019) were tackled (namely, the lack of specimen grinding before the cutting test, a non-constant test speed and problems with the displacement sensor), it should be object of slight changes to improve its structural rigidity, such as welding the steel plates. On the right side of the pneumatic cylinder used on the cutting machine, a space was purposely left to include a high-speed actuator to perform high speed cutting tests. Two linear guides were also placed in order to allow the machine's user to easily change actuators.

Relatively to the ring compression tests, as the roughness of the compression plates used was very low, only the effects of abrasion were studied on the tribological performance of maraging steel 18Ni300 under high temperature and strain rate conditions. Consequently, it is suggested that future students

and authors include the interlocking/ plastic deformation of asperities effect on the maraging steel's performance under these conditions. Another suggested future work is to evaluate the performance of different lubricants at different temperatures and strain rates using the ring compression tests, to assess the temperature and/or strain rate at which the lubricant starts to degrade.

Lastly, as the friction coefficients were found to have a clear variation with temperature and strain rate throughout the present work, it is suggested to investigate this variation on more materials, preferably on new engineering materials that lack experimental studies and characterization under different conditions.

7. References

Akiyama, T., Kishinami, T., Saito, K., & Hoshi, K. (1974). A Study Of The Orthogonal Cutting Mechanism By Controlled Shear Angle Experiments. *Memoirs Of The Faculty Of Engineering, Hokkaido University*, *14*(1), 13-20. Retrieved 30 October 2020, from http://hdl.handle.net/2115/37930.

Andrade, D. (2019). *Desenvolvimento de Aparato Experimental para Ensaios de Corte por Arranque de Apara,* (M.Sc. Thesis). Instituto Superior Técnico.

A, T., Ricks, J., Park, C., Tipper, C., & Luhrs, C. (2020). Mechanical Properties of 3D-Printed Maraging Steel Induced by Environmental Exposure. *Metals*, *10*(2), 218. https://doi.org/10.3390/met10020218

Asai, K., Kitamura, K., Yukawa, N., & Hayashi, N. (2017). Estimation of friction by using improved calibration curves of ring compression test for hot forging of steel. *Procedia Engineering*, *207*, 2280-2285. https://doi.org/10.1016/j.proeng.2017.10.995

Bay N. (1985). *Friction and Adhesion in Metal forming and Cold Welding*, (D.Sc. Thesis). Technical University of Denmark.

Bhukya, R., Rao, C., & Rao, G. (2014). Evaluation and comparison of Machinability characteristics of Maraging Steel and AISI 304 Steels. *5 Th International & 26Th All India Manufacturing Technology, Design And Research Conference (AIMTDR 2014)*, *473*,1-7.

Bhushan, B. (2003). Adhesion and stiction: Mechanisms, measurement techniques, and methods for reduction. *Journal Of Vacuum Science & Technology B: Microelectronics And Nanometer Structures*, *21*(6), 2262. https://doi.org/10.1116/1.1627336

Bonaiti, G., Parenti, P., Annoni, M., & Kapoor, S. (2017). Micro-milling Machinability of DED Additive Titanium Ti-6Al-4V. *Procedia Manufacturing*, *10*, 497-509. https://doi.org/10.1016/j.promfg.2017.07.104

Börder C. (2005). *Análise do coeficiente de atrito no ensaio de anel para o forjamento a quente*, (M.Sc. Thesis). Escola Politécnica da Universidade de São Paulo.

Bowden, F., & Tabor, D. (1964). *The friction and lubrication of solids*. Clarendon Press.

Brown E.D.,Owens R.S., Booser E.R. (1969). *Friction of Dry surfaces*, ASME, New York.

Cangundo E. (2009). *Avaliação experimental da condição tribológica no processo de corte por arranque de apara*, (M.Sc. Thesis). Instituto Superior Técnico.

Casati, R., Lemke, J., Tuissi, A., & Vedani, M. (2016). Aging Behaviour and Mechanical Performance of 18-Ni 300 Steel Processed by Selective Laser Melting. *Metals*, *6*(9), 218. https://doi.org/10.3390/met6090218

Carrilho J. (2009). *Avaliação experimental da força de atrito durante o processo de corte por arranque de apara*, (M.Sc. Thesis). Instituto Superior Técnico.

Cordeiro D. (2010). *Avaliação Numérica e Experimental de Tensões Residuais*, (M.Sc. Thesis). Instituto Superior Técnico.

Cristino V. (2007). *Experimental Assessment of Analytical Solutions for Orthogonal Metal Cutting*, (D.Sc. Thesis). Instituto Superior Técnico.

Cristino, V., Rosa, P., & Martins, P. (2011). Surface roughness and material strength of tribo-pairs in ring compression tests. *Tribology International*, *44*(2), 134-143. doi: 10.1016/j.triboint.2010.10.002

Dubois, J., & Belin-Ferré, E. (2014). Friction and solid-solid adhesion on complex metallic alloys. *Science And Technology Of Advanced Materials*, *15*(3), 034804. doi: 10.1088/1468-6996/15/3/034804

Fernandes J. (2017). *A importância do oxigénio no comportamento tribológico do corte por arranque de apara*, (M.Sc. Thesis). Instituto Superior Técnico.

Fletcher, J., Li, Y., Beynon, J., & Sellars, C. (1998). The influence of surface conditions in hot forming determined by ring upsetting: A numerical and experimental investigation. *The Journal Of Engineering Tribology*, *212*(6), 453-465. https://doi.org/https://doi.org/10.1243/1350650981542254

Fredriksson, C. (2019). Sustainability of metal powder additive manufacturing. *Procedia Manufacturing*, *33*, 139-144. https://doi.org/10.1016/j.promfg.2019.04.018

Fromentin, G., Gasparoux, J., Agbeviade, K., & Giovanola, J. (2016). Development of a precision machine to perform and study orthogonal micro-cutting. *Production Engineering*, *10*(2), 217-226. https://doi.org/10.1007/s11740-016-0657-8

Garmong, G., Paton, N., Chesnutt, J., & Nevarez, L. (1977). An evaluation of the ring test for strain-rate-sensitive materials. *Metallurgical Transactions A*, *8*(12), 2026-2027. https://doi.org/10.1007/bf02646583

Hartley, R., Cloete, T. and Nurick, G. (2007). An experimental assessment of friction effects in the split Hopkinson pressure bar using the ring compression test. *International Journal of Impact Engineering*, *34*(10), 1705-1728.

Heigel, J., Phan, T., Fox, J., & Gnaupel-Herold, T. (2018). Experimental Investigation of Residual Stress and its Impact on Machining in Hybrid Additive/Subtractive Manufacturing. *Procedia Manufacturing*, *26*, 929-940. https://doi.org/10.1016/j.promfg.2018.07.120

Kandibanda R. (2008). *Topology-based modeling and an -based modeling and analysis of or sis of orthogonal cutting process*, (M.Sc. Thesis). University of Kentucky.

Lee E. H. & Shaffer B.W. (1951), Theory of plasticity applied to a problem of machining*, J. appl. Mech.,* Trans. ASME, *73,* 405-413.

Lohmann, I., Sarvezuk, P., Ferreira, R., Ivashita, F., Da Cas Viegas, A., de Andrade, A., & Paesano, A. (2019). Maraging-300: a structural and hyperfine study of steel aging. *Hyperfine Interactions*, *240*(1). https://doi.org/10.1007/s10751-019-1566-y

Lopresto, V., Langella, A., Caprino, G., Durante, M., & Santo, L. (2017). Conventional Orthogonal Cutting Machining on Unidirectional Fibre Reinforced Plastics. *Procedia CIRP*, *62*, 9-14. https://doi.org/10.1016/j.procir.2016.07.036

Male, A.T., and Cockcroft, M.G. (1965). A method for the determination of the friction coefficient of metals under conditions of bulk plastic deformation, *Journal of the Institute of Metals*, *46,* 93-38.

Male, A. (1965). Variations in friction coefficients of Metals during Compressive Deformation. *Journal Of The Institute Of Metals*, *94*, 121-125.

Merchant M. E. (1945). Mechanics of the metal cutting process. I. Orthogonal cutting and a type 2 chip, J*. Appl. Phys., 16,* 267–275.

Miyoshi, K. (1995). Adhesion, Friction, and Wear Behavior of Clean Metal-Ceramic Couples. In *International Tribology Conference*. Cleveland, Ohio; NASA. Retrieved 29 October 2020, from https://ntrs.nasa.gov/citations/19950013367.

Montevecchi, F., Grossi, N., Takagi, H., Scippa, A., Sasahara, H., & Campatelli, G. (2016). Cutting Forces Analysis in Additive Manufactured AISI H13 Alloy. *Procedia CIRP*, *46*, 476-479. https://doi.org/10.1016/j.procir.2016.04.034

Opaliński, M., Mazuro, P., Klasik, A. and Rostek, E. (2016). Tribological Examination of Different Steel Materials after Special Heat Treatment and Salt Bath Nitriding. *Archives of Metallurgy and Materials*, *61*(4), 1881-1888.

Özel, T., & Altan, T. (2000). Determination of workpiece flow stress and friction at the chip–tool contact for high-speed cutting. *International Journal Of Machine Tools And Manufacture*, *40*(1), 133-152. https://doi.org/10.1016/s0890-6955(99)00051-6

Peng, C., Fu, Y., Wei, H., Li, S., Wang, X., & Gao, H. (2018). Study on Improvement of Surface Roughness and Induced Residual Stress for Additively Manufactured Metal Parts by Abrasive Flow Machining. *Procedia CIRP*, *71*, 386-389. https://doi.org/10.1016/j.procir.2018.05.046

Pereira J. (2009). *Análise Experimental e Modelação Numérica do Mecanismo de Formação de Apara em condições de corte ortogonal*, (M.Sc. Thesis). Instituto Superior Técnico.

Polishetty, A., Shunmugavel, M., Goldberg, M., Littlefair, G., & Singh, R. (2017). Cutting Force and Surface Finish Analysis of Machining Additive Manufactured Titanium Alloy Ti-6Al-4V. *Procedia Manufacturing*, *7*, 284-289. https://doi.org/10.1016/j.promfg.2016.12.071

Priarone P. C., Rizzuti S., Settineri L. and Vergnano G. (2012). Effects of cutting angle edge preparation and nano-structured coating on milling performance of a gamma titanium aluminide, *J. Mater. Process. Technol., 212*(12), 2619-2628.

Rahman M., Wong Y. S. and Zareena A. R. (2003). Machinability of titanium alloys*, JSME Int. J. Ser. C 46*, 107–114.

Rolled Alloys, I. (2020). *Machining - Rolled Alloys, Inc.*. Rolledalloys.com. Retrieved 30 October 2020, from https://www.rolledalloys.com/technical-resources/fabrication-information/machining.

Rudkins, N., Hartley, P., Pillinger, I., & Petty, D. (1996). Friction modelling and experimental observations in hot ring compression tests. *Journal Of Materials Processing Technology*, *60*(1-4), 349-353. https://doi.org/10.1016/0924-0136(96)02353-9

Santos S. (2005). *Influência dos principais parâmetros de corte na geometria da apara*, (M.Sc. Thesis). Instituto Superior Técnico.

Segebade, E., Gerstenmeyer, M., Dietrich, S., Zanger, F., & Schulze, V. (2019). Influence of anisotropy of additively manufactured AlSi10Mg parts on chip formation during orthogonal cutting. *Procedia CIRP*, *82*, 113-118. https://doi.org/10.1016/j.procir.2019.04.043

Shahriari, D., Sadeghi, M., Ebrahimi, G., & Kim, K. (2011). Effects of lubricant and temperature on friction coefficient during hot forging of Nimonic 115 superalloy. *Metallic Materials*, *49*(05), 375-383. https://doi.org/10.4149/km_2011_5_375

Shokrani, A., Dhokia, V., & Newman, S. (2016). Cryogenic High Speed Machining of Cobalt Chromium Alloy. *Procedia CIRP*, *46*, 404-407. https://doi.org/10.1016/j.procir.2016.04.045

Shunmugesh, K., & Panneerselvam, K. (2016). Machinability study of Carbon Fiber Reinforced Polymer in the longitudinal and transverse direction and optimization of process parameters using PSO–GSA. *Engineering Science And Technology, An International Journal*, *19*(3), 1552-1563. https://doi.org/10.1016/j.jestch.2016.04.012

Steeds W. (1969). *A History of Machine Tools,* Clarendon Press.

Stephenson, D. & Agapiou, J. (2016). *Metal Cutting Theory and Practice*. CRC Press.

Sun, S., Brandt, M. & Dargusch, M. (2009). Characteristics of cutting forces and chip formation in machining of titanium alloys*. International Journal of Machine Tools and Manufacture*, *49*(7-8), 561–568.

Sun, K., Peng, W., Wei, B., Yang, L. and Fang, L. (2020). Friction and Wear Characteristics of 18Ni(300) Maraging Steel under High-Speed Dry Sliding Conditions. *Materials 2020*, *13*(7), 1485-1495.

Thimm, B., Glavas, A., Reuber, M., & Christ, H. (2020). Determination of chip speed and shear strain rate in primary shear zone using digital image correlation (DIC) in linear-orthogonal cutting

experiments. *Journal Of Materials Processing Technology*, *289*, 116957. https://doi.org/10.1016/j.jmatprotec.2020.116957

Vikhareva, A. (2020). *Tribological characterization of additively manufactured hot forming steels,* (M.Sc. Thesis). Luleå University of Technology.

Wegener, K., Kuster, F., Weikert, S., Weiss, L., & Stirnimann, J. (2016). Success Story Cutting. *Procedia CIRP*, *46*, 512-524. https://doi.org/10.1016/j.procir.2016.04.110

Yin, S., Chen, C., Yan, X., Feng, X., Jenkins, R., O'Reilly, P., Liu, M., Li, H. and Lupoi, R. (2018). The influence of aging temperature and aging time on the mechanical and tribological properties of selective laser melted maraging 18Ni-300 steel. *Additive Manufacturing*, *22,* 592-600.

Attachments

A.I – Developed MATLAB code to perform the subtraction of stress-strain curves

A.II – Corrected stress-strain curves

A.III – Lubricated ring compression tests full results

A.IV – Dry ring compression tests full results

A.V – Standard ring compression tests measurements sheet used

A.VI – Cutting machine’s data acquisition manual

A.VII – Low speed orthogonal cutting procedures manual

A.VIII – Developed Labview program

A.I - Developed MATLAB code to perform the subtraction of stress-strain curves

```
function [extensao_final, tensao_final] = subrator

ficheiro = input('Introduza o nome do ficheiro 1: ','s');
ficheiro_2 = input('Introduza o nome do ficheiro 2: ','s');
grau_polinomio = input('Insira o grau do polinomio interpolador do ficheiro
1: ');
grau_polinomio_1 = input('Insira o grau do polinomio interpolador do
ficheiro 2: ');
numero_pontos = input('Insira o numero de pontos que deseja obter no
ficheiro de output: ');
dados_1 = fopen (ficheiro, 'rt');

if dados_1 == -1
    disp('\nErro na abertura do ficheiro!\n\n');
else

    % Leitura do 1o ficheiro xls

    matriz_dos_dados = xlsread(ficheiro);
    extensao = matriz_dos_dados(:,1);
    tensao = matriz_dos_dados(:,2);

    % Reducao vetor extensao

    maximo_extensao = max(extensao);
    minimo_extensao = min(extensao);
    range_extensao = maximo_extensao - minimo_extensao;
    passo_extensao = range_extensao / numero_pontos;

    % Inicializacao

    i = 1;
    j = 1;
    k = 1;
    extensao_final = zeros(numero_pontos,1);
    extensao_final_pl = zeros(numero_pontos,1);

    while i <= numero_pontos

        if i == 1

            extensao_final(1) = extensao(1);
            extensao_final_pl(1) = 0;

        else

            extensao_final(i) = extensao_final(i-1) + passo_extensao;
            extensao_final_pl(i) = extensao_final_pl(i-1) + passo_extensao;

        end

        i = i + 1;
```

```
    end

    % Polinomio interpolador

   coeficientes = polyfit(extensao, tensao, grau_polinomio);
   tensao_final = polyval(coeficientes, extensao_final);
   %tensao_final = interp1(extensao,tensao,extensao_final);

dados_2 = fopen (ficheiro_2, 'rt');

if dados_2 == -1
    disp('\nErro na abertura do ficheiro!\n\n');
else

    % Leitura do 2o ficheiro xls

    matriz_dos_dados = xlsread(ficheiro_2);
    extensao_2 = matriz_dos_dados(:,1);
    tensao_2 = matriz_dos_dados(:,2);

    % Reducao vetor extensao

    maximo_extensao = max(extensao_2);
    minimo_extensao = min(extensao_2);
    range_extensao = maximo_extensao - minimo_extensao;
    passo_extensao = range_extensao / numero_pontos;

    % Inicializacao

    i = 1;
    j = 1;
    k = 1;
    l = 1;
    extensao_final_2 = zeros(numero_pontos,1);

    while i <= numero_pontos

        if i == 1

            extensao_final_2(1) = extensao_2(1);

        else

            extensao_final_2(i) = extensao_final_2(i-1) + passo_extensao;

        end

        i = i + 1;

    end

    % Polinomio interpolador

    coeficientes_2 = polyfit(extensao_2, tensao_2, grau_polinomio_1);
    tensao_final_2 = polyval(coeficientes_2, extensao_final_2);
    %tensao_final_2 = interp1(extensao_2,tensao_2,extensao_final_2);
```

```
end

% Subtrair graficos

tensao_subtraida_0 = zeros(numero_pontos,1);
tensao_subtraida = zeros(numero_pontos,1);

i = 1;

while i <= numero_pontos

    tensao_subtraida_0(i) = tensao_final(i) - tensao_final_2(i);
    tensao_subtraida(i) = tensao_final_2(i) - tensao_subtraida_0(i);

    i = i + 1;

end

% Apresentar grafico

plot(extensao_final,tensao_subtraida);

% Valor maximo entre curvas

dist_max = max(tensao_subtraida_0);
media = mean(tensao_subtraida_0);
disp(dist_max);
disp(media);

% Ficheiros de output

fid_1 = fopen('extensao.txt', 'wt');

while j <= numero_pontos

    extensao_final_1 = num2str(extensao_final(j,1));
    extensao_final_0 = strrep(extensao_final_1, '.', ',');
    fprintf(fid_1, '%s \n', extensao_final_0);

    j = j + 1;

end

fclose(fid_1);

fid_2 = fopen('tensao.txt', 'wt');

while k <= numero_pontos

    tensao_final_1 = num2str(tensao_subtraida(k,1));
    tensao_final_0 = strrep(tensao_final_1, '.', ',');
    fprintf(fid_2, '%s \n', tensao_final_0);

    k = k + 1;

end
```

```
fclose(fid_2);

fid_3 = fopen('extensao_pl.txt', 'wt');

while l < numero_pontos

    extensao_final_pl_1 = num2str(extensao_final_pl(l,1));
    extensao_final_pl_0 = strrep(extensao_final_pl_1, '.', '.');
    fprintf(fid_3, '%s \n', extensao_final_pl_0);

    l = l + 1;

end

fclose(fid_3);

end

end
```

A.II – Corrected stress-strain curves

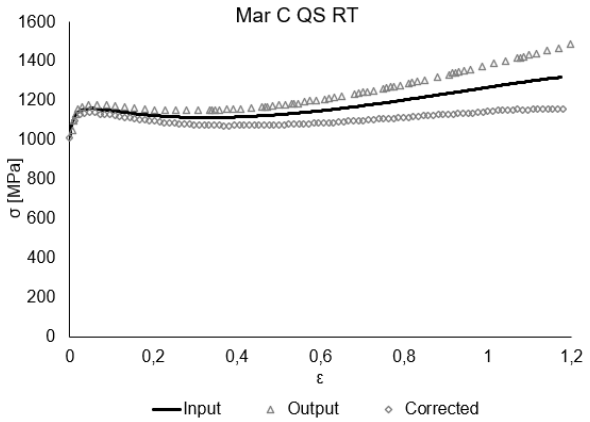

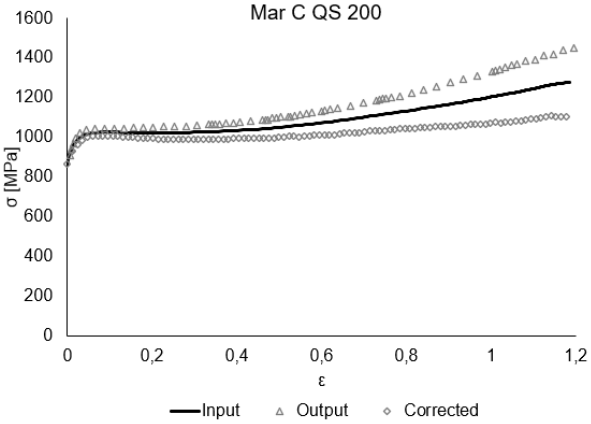

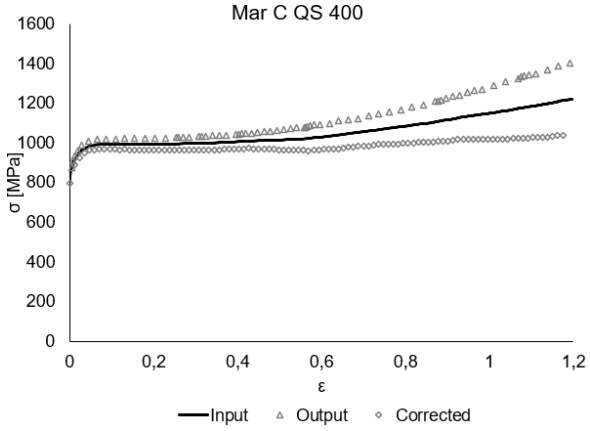

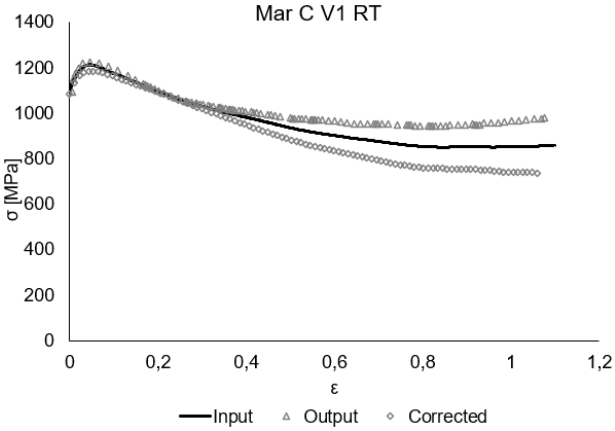

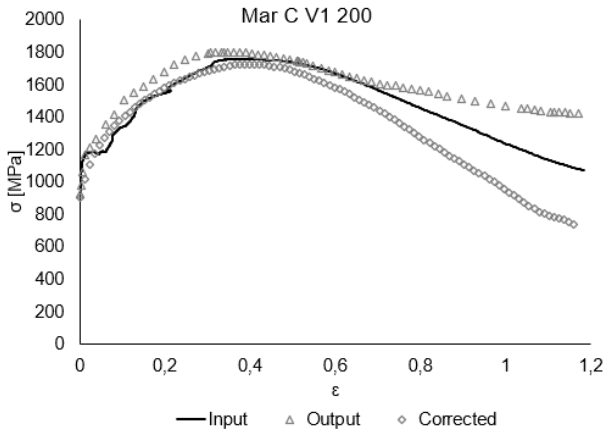

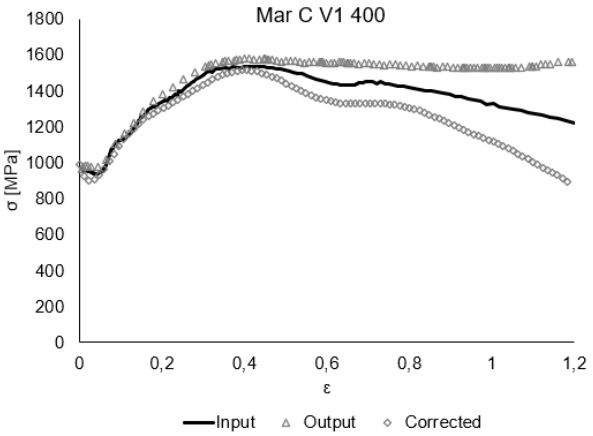

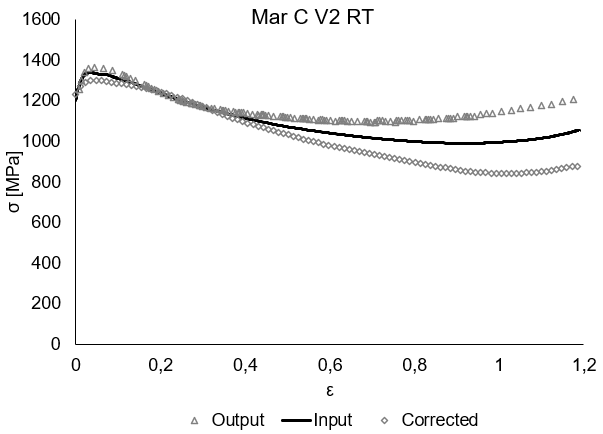
Mar C V2 RT
σ [MPa]
ε
Output
Input
Corrected

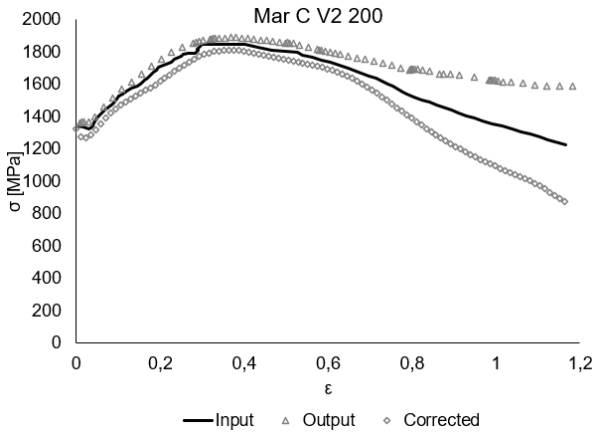
Mar C V2 200
σ [MPa]
ε
Input
Output
Corrected

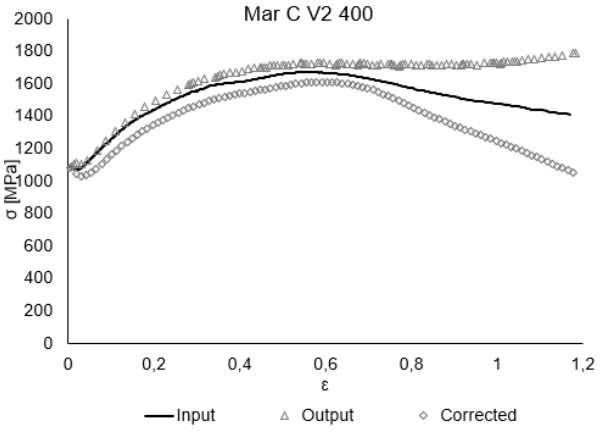
Mar C V2 400
σ [MPa]
ε
Input
Output
Corrected

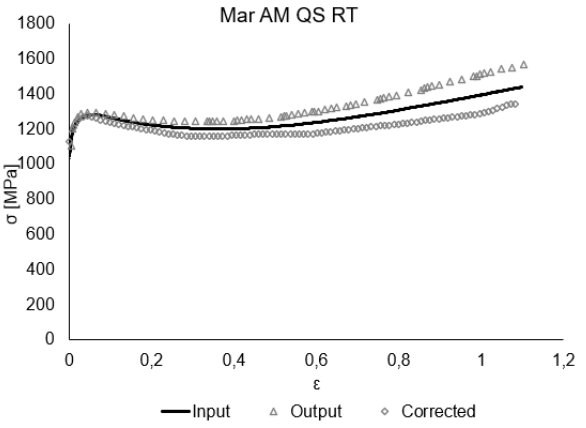
Mar AM QS RT
σ [MPa]
ε
Input
Output
Corrected

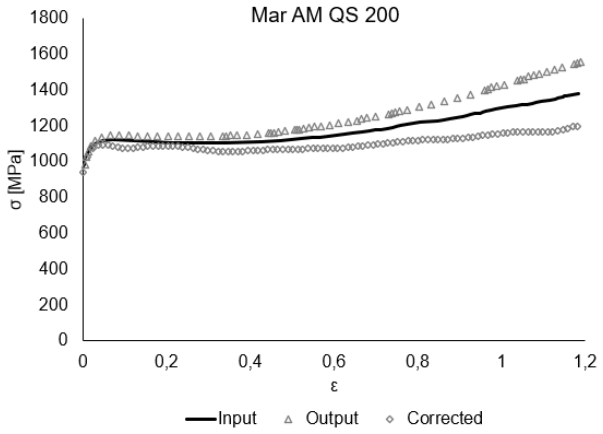
Mar AM QS 200
σ [MPa]
ε
Input
Output
Corrected

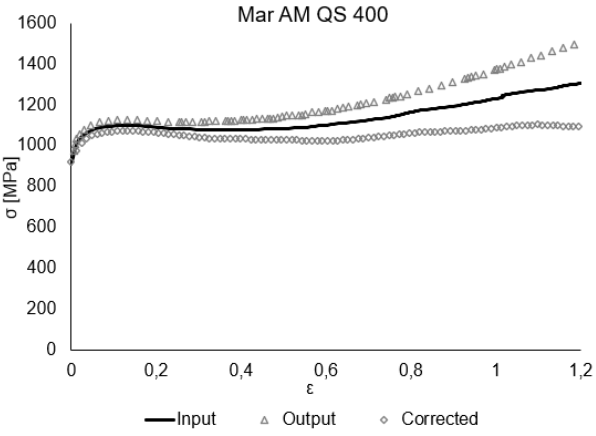
Mar AM QS 400
σ [MPa]
ε
Input
Output
Corrected

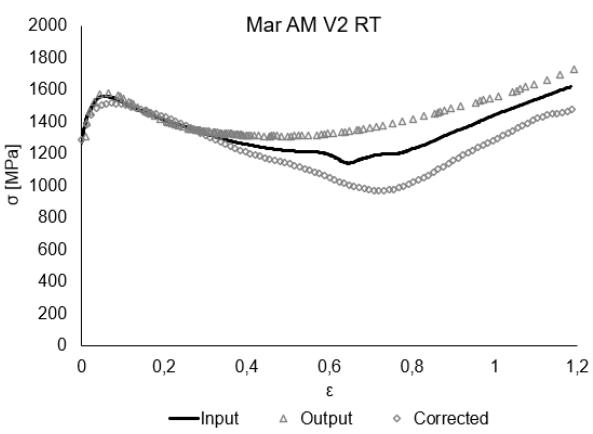
Mar AM V2 RT
σ [MPa]
ε
Input
Output
Corrected

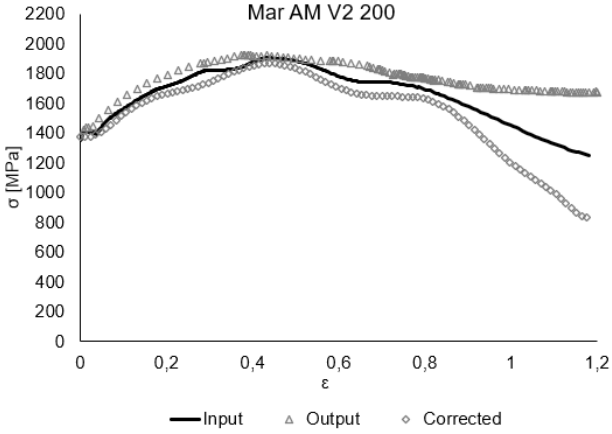
Mar AM V2 200
σ [MPa]
ε
Input
Output
Corrected

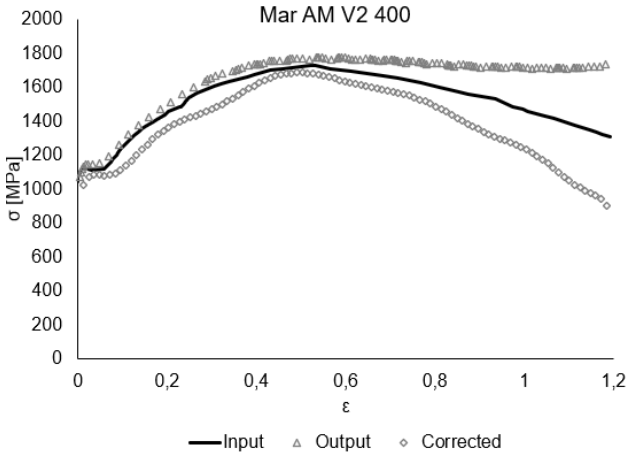
Mar AM V2 400
σ [MPa]
ε
Input
Output
Corrected

A.III – Lubricated ring compression tests results

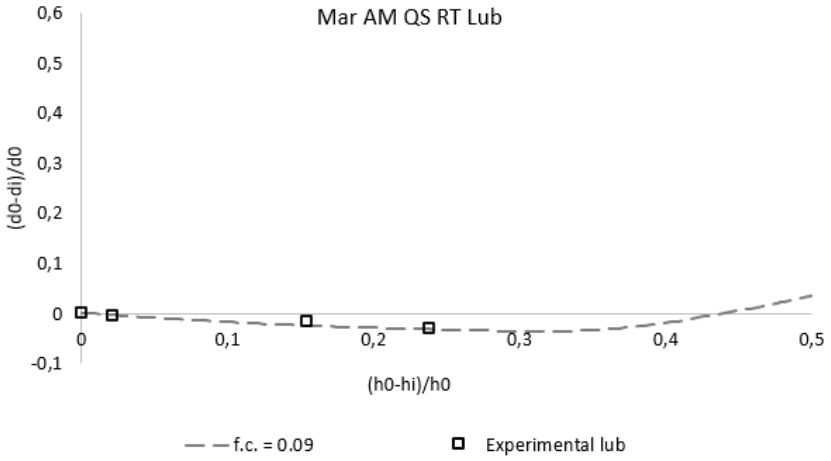

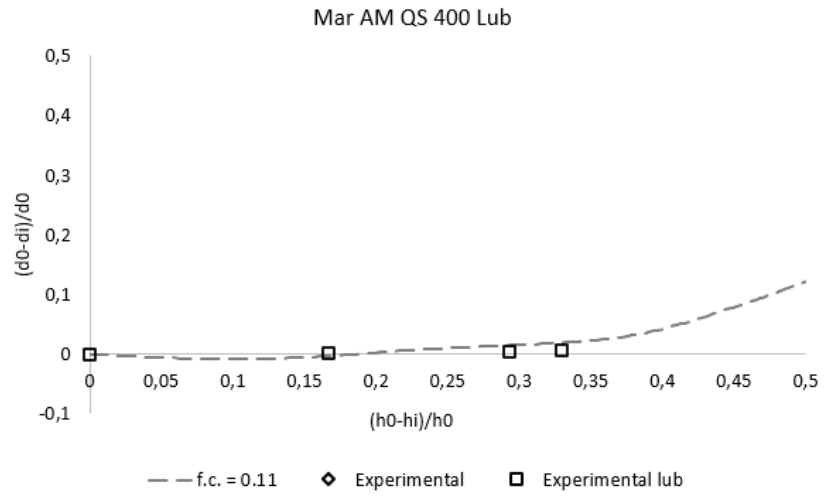

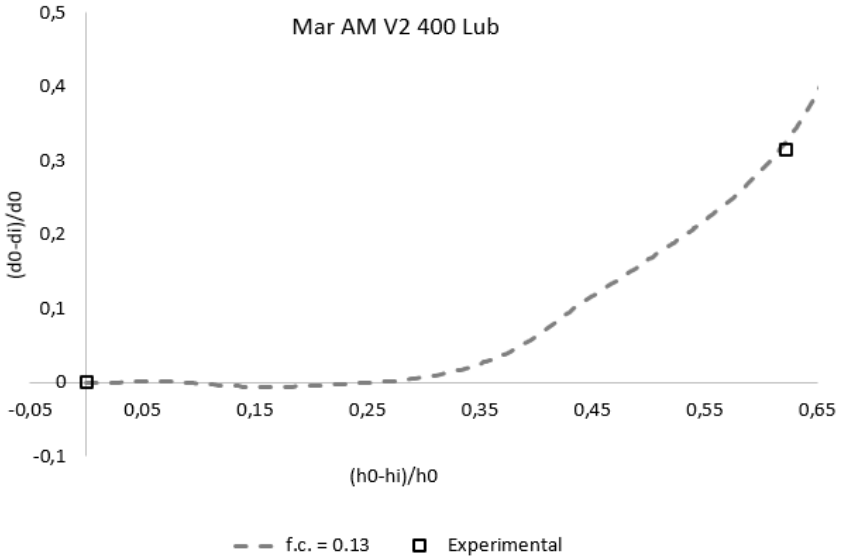

A.III – Dry ring compression tests results

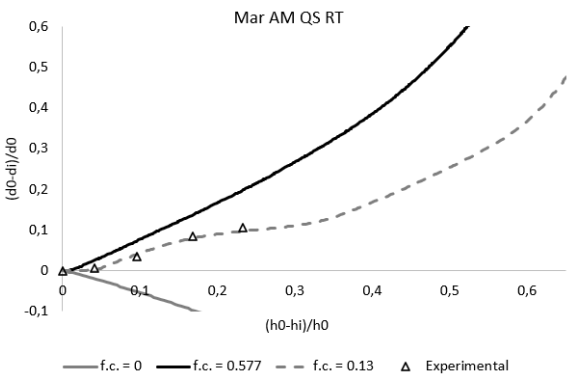

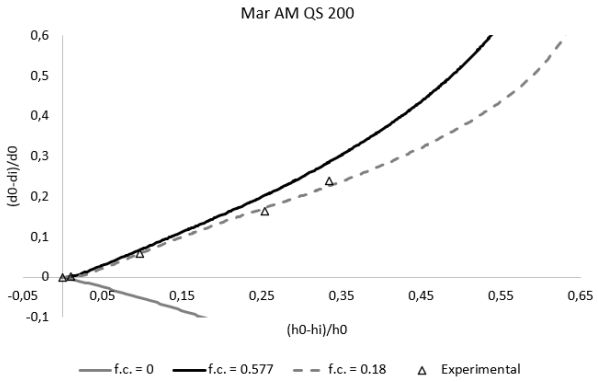

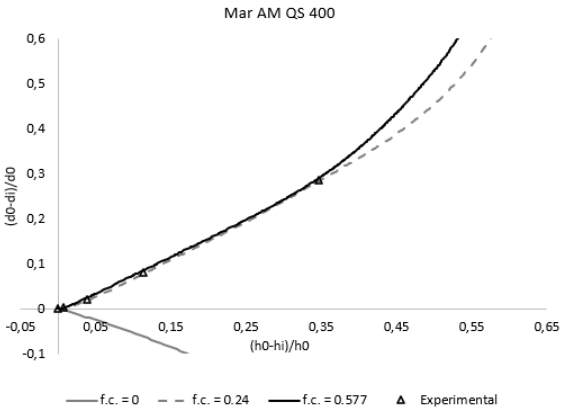

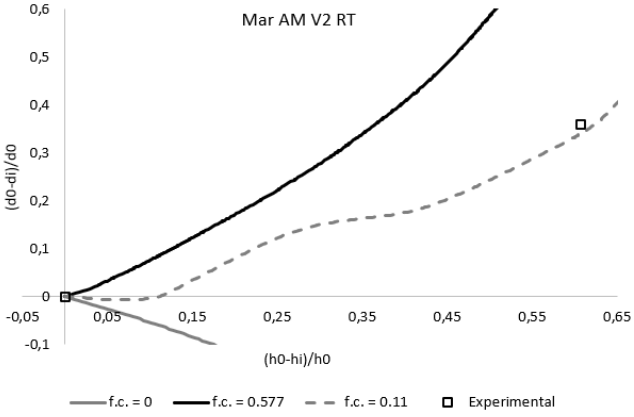

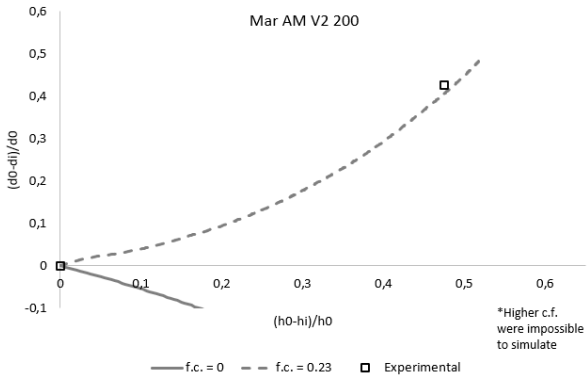

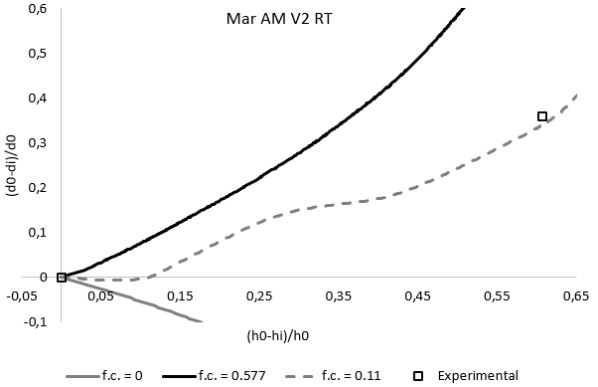

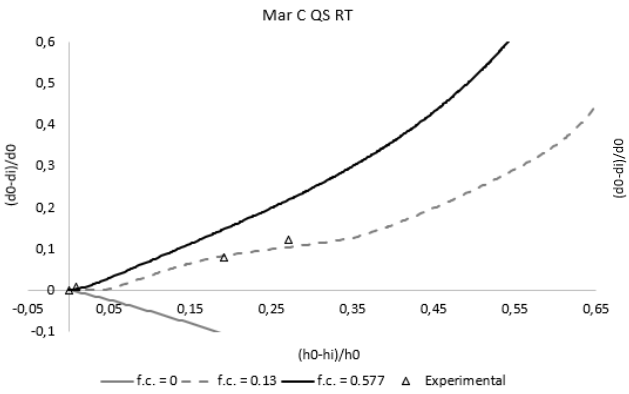
Mar C QS RT
(d0-di)/d0
(h0-hi)/h0
f.c. = 0
f.c. = 0.13
f.c. = 0.577
Experimental

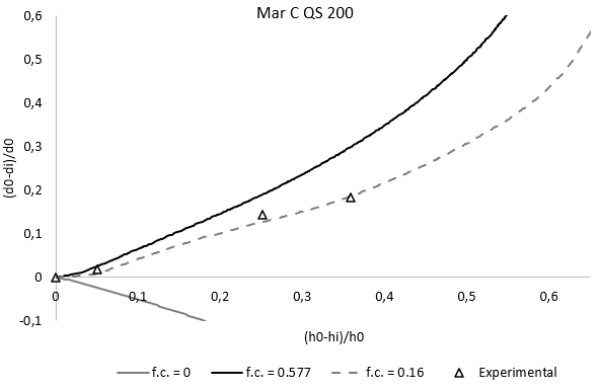
Mar C QS 200
(d0-di)/d0
(h0-hi)/h0
f.c. = 0
f.c. = 0.577
f.c. = 0.16
Experimental

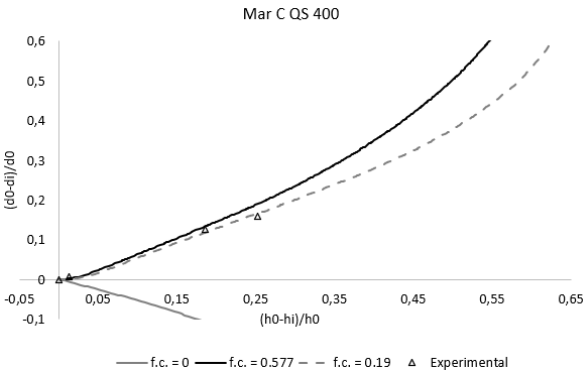
Mar C QS 400
(d0-di)/d0
(h0-hi)/h0
f.c. = 0
f.c. = 0.577
f.c. = 0.19
Experimental

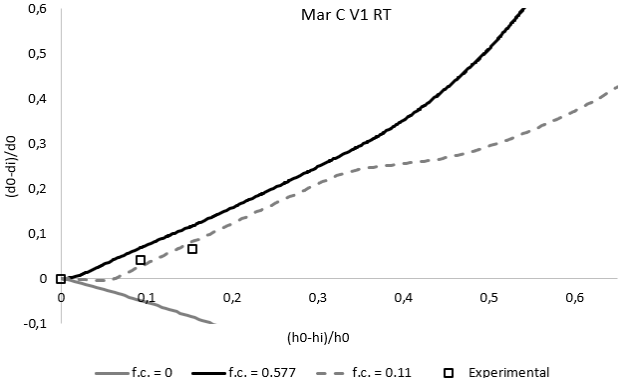
Mar C V1 RT
(d0-di)/d0
(h0-hi)/h0
f.c. = 0
f.c. = 0.577
f.c. = 0.11
Experimental

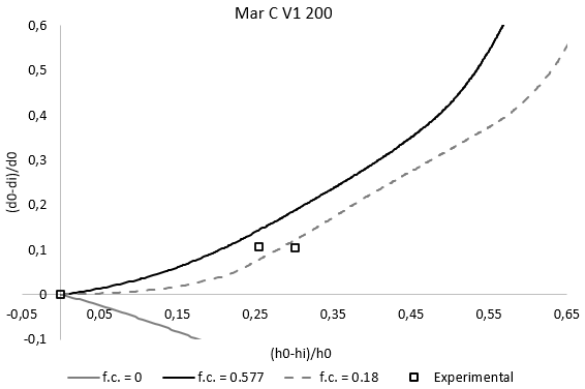
Mar C V1 200
(d0-di)/d0
(h0-hi)/h0
f.c. = 0
f.c. = 0.577
f.c. = 0.18
Experimental

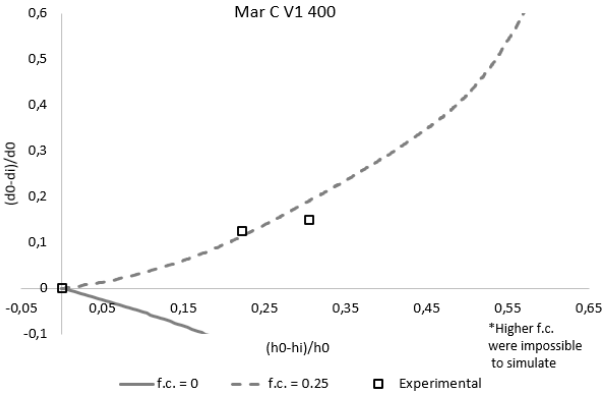
Mar C V1 400
(d0-di)/d0
(h0-hi)/h0
*Higher f.c.
were impossible
to simulate
f.c. = 0
f.c. = 0.25
Experimental

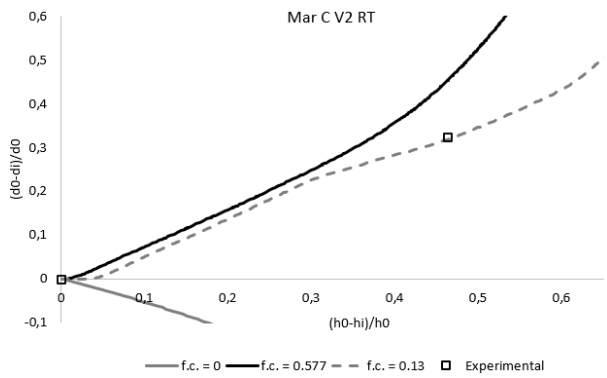
Mar C V2 RT
(d0-di)/d0
(h0-hi)/h0
f.c. = 0
f.c. = 0.577
f.c. = 0.13
Experimental

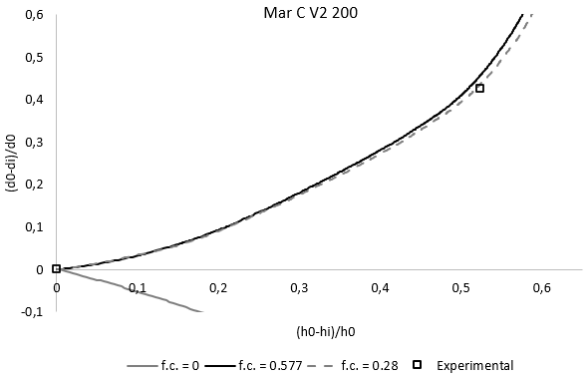
Mar C V2 200
(d0-di)/d0
(h0-hi)/h0
f.c. = 0
f.c. = 0.577
f.c. = 0.28
Experimental

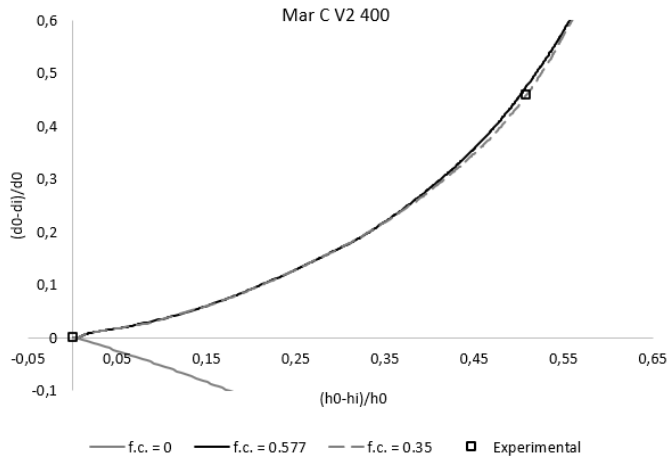
Mar C V2 400
(d0-di)/d0
(h0-hi)/h0
f.c. = 0
f.c. = 0.577
f.c. = 0.35
Experimental

A.V – Standard ring compression tests measurements sheet used

Ensaio nº	h0 [mm]	ϕext [mm]	ϕint [mm]	Pressão [bar]	Tipo	T [ºC]	Lub

A.VI – Cutting machine's data acquisition manual

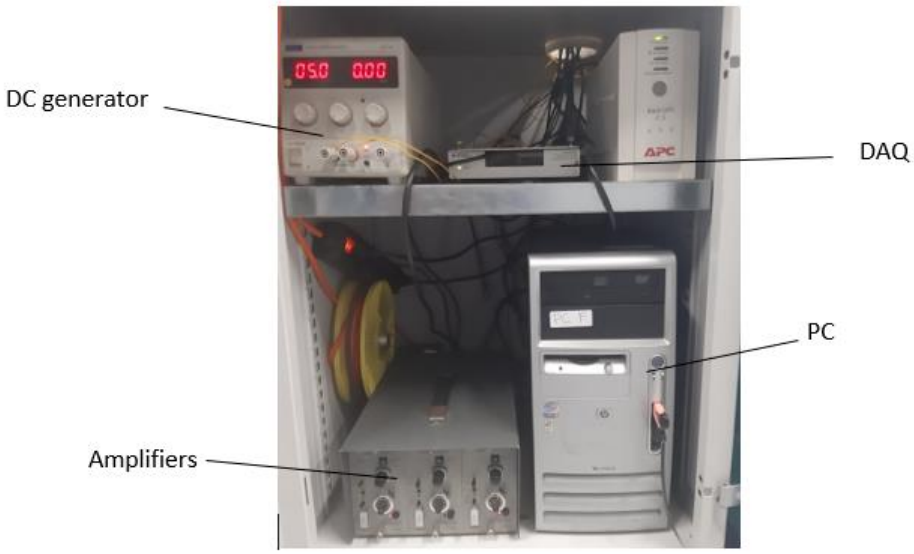

1) Turn on the pc and monitor
2) Turn on the data acquisition system (DAQ)
3) Turn on the first and third modules of the amplifier
4) Turn on the DC generator, and make sure it is calibrated to 5V
5) On the pc, open the folder "Tese João Coelho", and then the program "Duarte canhao"
6) Wait half an hour before performing a cutting test
7) When ready to perform the test, put the dark lever on the amplifier modules on "reset", and then "operate" – figure 1
8) On the program, choose the save directory (on the yellow folder), and then hit the "Gravar" button – figure 2
9) When the light turns green, perform your experiment. When the test is done, hit the "Gravar" button again, and see if the folder containing your data is inside the folder you have chosen before

Figure 1

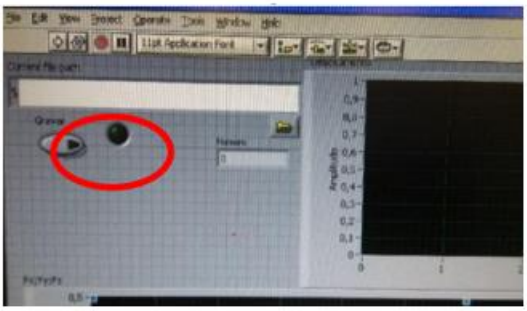

Figure 2

A.VII – Low speed orthogonal cutting procedures manual

1) Make sure the tool's rake face above the specimen
2) Adjust the micrometric screw until the tool touches the specimen – figure 1
3) Loose the cutting tool by unscrewing the 5 screws shown on figure 2
4) Pull the specimen up (using the rack pinion mechanism at the bottom of the machine), until it is no longer below the tool
5) Choose the depth of cut (using the micrometric screw)
6) Tighten the screw through the same screws referred on step 3
7) Make sure you put the white plastic part on the lateral screw that holds the specimen, so that the displacement sensor can work along the cutting process – figure 3
8) You can now perform the test

Figure 1

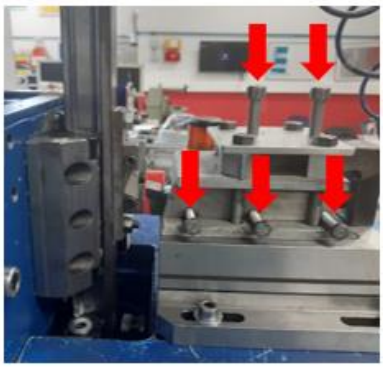

Figure 2

Figure 3

A.VIII – Developed Labview program